Shaping memory with magnesium
–
how moderate activation of LFA-1 with magnesium optimizes $CD8^+$ T cell effector function

Inauguraldissertation

zur

Erlangung der Würde eines Doktors der Philosophie

vorgelegt der
Philosophisch-Naturwissenschaftlichen Fakultät
der Universität Basel

von
Jonas Lötscher

2022

Genehmigt von der Philosophisch-Naturwissenschaftlichen Fakultät

auf Antrag von

Prof. Dr. Dr. Christoph Hess

Prof. Dr. Christoph Handschin

Prof. Dr. Ping-Chih Ho

Basel, den 13.10.2020

Prof Dr. Martin Spiess

Dekan

TABLE OF CONTENTS

Acknowledgments	4
Summary	6
Introduction	7
Results	9
Discussion	33
Material and Methods	36
Supplemental Material	52
References	67
Curriculum Vitae	72

ACKNOWLEDGEMENTS

My PhD study has been a very exciting, intense and educational journey – an experience I would not want to miss anymore. During these years I have received a great deal of support from various people and I want to express my gratitude to all of those who have helped me with their experimental work, guidance, ideas and friendship.

Above all, I want to thank my supervisor, Christoph Hess, for his great and continuous support during my PhD. His enthusiasm for science, broad knowledge and supportive energy were of invaluable help and motivation. Furthermore, I highly appreciated his open-door policy, incredible working efficiency and scientific guidance. Without him this work would not have been possible.

During the daily work I was accompanied by the great team of the *Immunobiology Laboratory*. My sincere thank goes to all present and former Lab members, Nadine Assmann, Maria Balmer, Glen Bantug, Anne-Valérie Burgener, Philippe Dehio, Bojana Durovic-Müller, Raja Epple, Marco Geiges, Jasmin Grählert, Patrick Gubser, Jessica Jäger, Tamara Kellerhals, Dahye Lee, Jordan Löliger, Sarah Roffeis, Rebekkah Steiner, Sabine Tschirren and Gunhild Unterstab. Special thanks go to Maria who helped me a lot and was a great mentor. Furthermore, I want to express my gratitude to my "twin" Jordan, Philippe, Anne-Valérie and Jasmine for their friendship and support.

This work would not have been possible without great collaborators. I am sincerely grateful for the help with the intra-tumor injection experiments which was a huge experimental effort of Adrià-Arnau Marti Lindez and Walter Reith from the University of Geneva.
I would like to give my credits to Elisabetta Cribrioli, Greta Giordano-Attianese and Melita Irving from the University of Lausanne for their help with the *in-vivo* CAR T cell experiments.
My sincere thanks go to Marcel Trefny, Nicole Kirchhammer and Alfred Zippelius from the University of Basel for their time, generosity and excellent support with numerous aspects and experiments of the present thesis.
Furthermore, I want to thank Marco Künzli, Ludivine Litzler, David Schreiner and Carolyn King from the University of Basel for their help and efforts with flow cytometry and histology.
I am also grateful to Paolo Strati from the MD Anderson Cancer Center, Houston, for granting us access to the CAR T cell data-set.

I greatly appreciated the help and support from the members of the Lab 310 during daily work and joint lab meetings. A special thanks goes to Benedikt Meyer for his friendship.

I would further like to acknowledge the members of my thesis committee Christoph Hess, Christoph Handschin and Ping-Chih Ho for valuable advice during committee meetings and their willingness to review this thesis.

Furthermore, I thank Tobias Müller, Aron Strub, Milo Strub and Simon Wüthrich for many years of friendship and numerous funny moments which always helped to forget failed experiments.

Last but not least, I want to express my greatest gratitude to Isabelle Vock, my parents Monika and Pius Lötscher-Schmid and my brother Fabian Lötscher for their continuous support, wise guidance, great patience and love. Fluffy Julius shall also be thanked for being cute and a little bit featherheaded.

SUMMARY

While intracellular magnesium (Mg^{2+}) plays established and important roles in key cellular processes, the biologic relevance of extracellular Mg^{2+} remains largely unknown.

Here we show that in Mg^{2+}-rich environments $CD8^+$ T cell mediated cancer- and infection control were both improved. Surprisingly therefore, extracellular Mg^{2+} was distinctly compartmentalized across anatomic sites, creating naturally Mg^{2+} deplete tissues. Moderate activation of LFA-1 was underpinning Mg^{2+}-mediated improvement of $CD8^+$ T cell functionality by supporting: Ca^{2+} flux; signal transduction; cell activation; metabolic reprogramming; immune synapse formation and specific cytotoxic activity. Blocking LFA-1, excessive LFA-1 stabilization, as well as overriding LFA-1 signaling all hindered optimal $CD8^+$ T cell function. This principle translated to the performance of CAR T cells, *in vitro* and *in vivo*, and low serum Mg^{2+} levels were associated with more rapid disease progression and poor survival in CAR T cell treated patients.

Mg^{2+} thus operates as a site-specific modulator of $CD8^+$ T cell immunity. Specifically, moderate stabilization of LFA-1 with Mg^{2+} was hitting an unrecognized sweet spot optimizing $CD8^+$ T cell effector function. This insight has important implications for efforts to harness the Mg^{2+}–LFA-1 axis for immunotherapy.

INTRODUCTION

After calcium, magnesium (Mg^{2+}) is the second most abundant cation in the mammalian organism, with a total body content of approximately 700 g in an adult human. More than half of the Mg^{2+} is fixed in bone tissue, either as integral part of the bone crystal, on the surface of hydroxyapatite or in the crystal's hydration shell [1,2]. Of the remainder, around 97% is intracellular – leaving only 3% in the extracellular fluid, 40% of which is bound to proteins [3]. Intracellular Mg^{2+} has many key functions, such as stabilizing ATP and cellular membranes, or as a cofactor of enzymes [3,4]. In $CD4^+$ T cells specifically, Mg^{2+} has been shown to modulate activity of an important kinase, ITK, and, accordingly, depletion intracellular Mg^{2+} negatively impacted $CD4^+$ T cell function upon activation [5]. The biologic importance of Mg^{2+} in the extracellular space, on the other hand, remains ill characterized.

In clinical medicine, low dietary Mg^{2+} intake and hypomagnesemia have been implicated in the pathophysiology of various diseases, including osteoporosis, hypertension, metabolic syndrome and cardiovascular disease, but also infection and cancer [6-13]. The estimated prevalence of hypomagnesemia in the general population is reported to be as high as 2,5%, increasing to 10% in patients admitted to a geriatric facility, 10%-20% in hospitalized patients, and up to 60% among the critically ill [14-19]. In intensive care population, hypomagnesemia has been associated with a higher prevalence of septic shock [20]. Only limited experimental data is available that explored how organismal Mg^{2+} abundance may affect the immune system. It has been reported, however, that in Mg^{2+}-deficient mice (i) metastatic spread of lung carcinoma cells injected subcutaneously was accelerated [21], and (ii) immune responses against influenza were impaired due to insufficient IL-2–inducible T cell kinase (ITK) activity [5]. Inversely, keeping rats on a Mg^{2+}-low diet resulted in reduced severity in autoimmune arthritis model [22]. Whether, in these models, an extracellular biologic role of Mg^{2+} was contributing to shaping adaptive immune responses has not been assessed.

$CD8^+$ T cells are a key component of the adaptive immune system, playing a critical role in identifying and eliminating malignantly transformed or infected cells. Memory $CD8^+$ T cells comprise a small population of antigen-experienced long-lived immune cells, able to acquire effector function more rapidly than their antigen naïve counterparts. Effector-memory (EM) $CD8^+$ T cells, which survey peripheral tissues for reappearance of cognate antigen, are particularly poised to engage in cytotoxic activity as they contain preformed perforin [23]. The process of targeted cytotoxicity is initiated through engagement of the T cell receptor (TCR) with its cognate peptide presented through MHC I. This interaction triggers formation of an immune synapse, which is a tight and highly organized, multimolecular interface between the T cell and its target cell [24,25]. At this transient synapse structure, cytotoxic granules, containing perforin and proteolytic enzymes, are released into the cytoplasm of the target cell, thereby initiating apoptosis [25,26].

Immune-surveillance of peripheral tissues is a metabolically challenging task requiring adaptation to constantly changing microenvironments, highly variable in nutrient-, mineral- and oxygen-content [27,28]. It could also be speculated that at least aspects of such restrictive microenvironments have specifically evolved to regulate select functions of immune cells in a compartment-specific manner [29]. In cancerous or infected tissues, immune cells are, in addition, competing with malignant cells and pathogens, respectively, for limited resources – further accentuating metabolic restriction which can impact their function [30].

In my PhD thesis I aimed to explore the functional, molecular and potential translational relevance of extracellular Mg^{2+} in shaping $CD8^+$ T cell function.

RESULTS

Intratumoral magnesium injections improve memory $CD8^+$ T cell mediated antitumor immunity

To explore the role of Mg^{2+} in the tumor microenvironment, and specifically its functional impact on T cell immunity, we examined the effect of intratumoral (i.t.) Mg^{2+} administration in the MC38-OVA tumor model. Specifically, mice were either immunized against ovalbumin (OVA), or left untreated, before subcutaneous injection of OVA-expressing MC38 colorectal carcinoma cells bilaterally on the flanks. From day 7 onwards, right-side tumors were repeatedly injected with 3 mM $MgCl_2$, whereas 3 mM solution of NaCl was injected into left-side tumors (**Figure 1a**, *Experimental Scheme*). In non-immunized mice, tumor growth was comparable between $MgCl_2$ and NaCl conditions (**Figure 1b**, *left panel*). By contrast, in mice harboring OVA-specific memory T cells, intra-tumoral $MgCl_2$ administration significantly reduced tumor growth – indicating that increasing intratumoral Mg^{2+} abundance was improving T cell immunity specifically of memory cells (**Figure 1b**, *right panel*). Next, we aimed to assess how combining $MgCl_2$ with PD1 blockade was impacting tumor-directed memory $CD8^+$ T cell function (**Figure 1c**, *Experimental Scheme*). Tumor control in mice receiving both intratumoral MgCl2 as well as PD-1 blockade was markedly superior compared to all other treatment regimens, with $MgCl_2$ alone again also improving immune control (**Figure 1d**). Aligning with the tumor growth data, survival of animals injected up to day 26 with $MgCl_2$, was significantly improved compared to the NaCl injected control group, both as sole intervention and when combined with PD1 blockade (**Figure 1e**).

Given the unexpected benefit of increasing local Mg^{2+} abundance for memory $CD8^+$ T cell mediated cancer control, we further characterized tumor-infiltrating $CD8^+$ T cells between treatment groups, using flow-cytometry. No significant differences in cell numbers of total and antigen-specific $CD8^+$ T cells infiltrating the tumor were detected (**Suppl. Figure 1a**,**b**). Likewise, cell numbers of total and antigen-specific $CD8^+$ T cells were comparable in tumor-draining lymph nodes (DLN) (**Suppl. Figure 1c**,**d**). In line with these data, the percentage of Ki-67 expressing antigen-specific $CD8^+$ T cells was also not different between groups (**Suppl. Figure 1e**,**f**). Mg^{2+} thus did not mediate its effect on tumor growth through increasing numbers or proliferation of tumor infiltrating memory $CD8^+$ T cells. However, preliminary microscopic analyses of cancer tissue revealed that in Mg^{2+} injected tumors, $CD8^+$ T cells had a more scattered spatial distribution when compared to control samples. Furthermore, expression of activation markers on $CD8^+$ T cells tended to be higher in Mg^{2+} injected tumors, while in tumor cells Ki67 – a marker of cell proliferation – was less abundant (data not shown). Notably therefore, when restimulated *ex vivo* using PMA and ionomycin, tumor infiltrating $CD8^+$ T cells produced comparable amounts of IFN-γ and similarly upregulated CD107a across treatment groups (**Suppl. Figure 1g**-**j**). This suggested to us that, if intratumoral Mg^{2+} was directly affecting infiltrating

memory $CD8^+$ T cells, its effect was transient in nature and/or overcome by supra-physiologic activation.

In all these experiments identified Mg^{2+} as an important modulator of memory $CD8^+$ T cell-dependent tumor control.

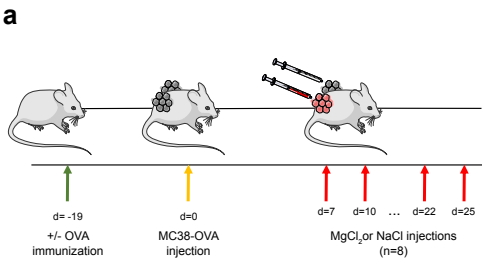
a
d= -19
+/- OVA immunization
d=0
MC38-OVA injection
d=7
d=10
…
d=22
d=25
MgCl2 or NaCl injections (n=8)

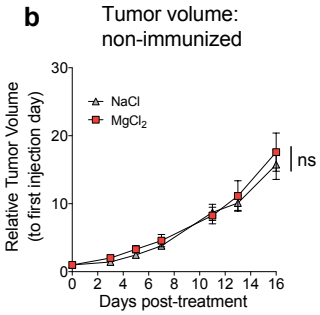
b
Tumor volume: non-immunized
Relative Tumor Volume (to first injection day)
NaCl
MgCl2
ns
Days post-treatment

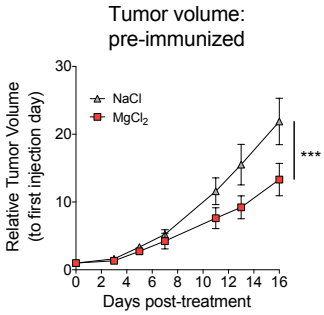
Tumor volume: pre-immunized
Relative Tumor Volume (to first injection day)
NaCl
MgCl2
***
Days post-treatment

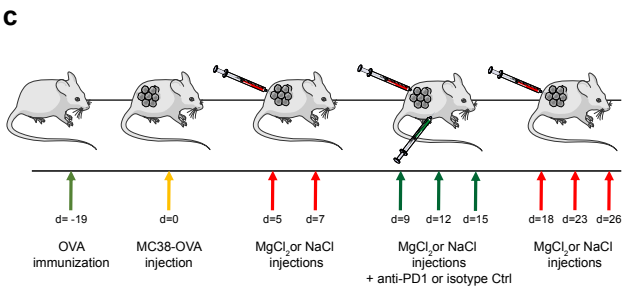
c
d= -19
OVA immunization
d=0
MC38-OVA injection
d=5
d=7
MgCl2 or NaCl injections
d=9
d=12
d=15
MgCl2 or NaCl injections + anti-PD1 or isotype Ctrl
d=18
d=23
d=26
MgCl2 or NaCl injections

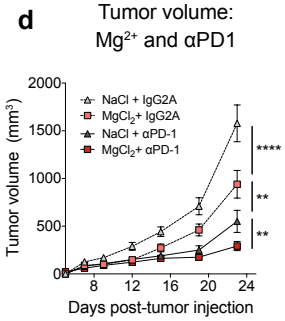
d
Tumor volume: Mg2+ and αPD1
Tumor volume (mm3)
NaCl + IgG2A
MgCl2 + IgG2A
NaCl + αPD-1
MgCl2 + αPD-1
****
**
**
Days post-tumor injection

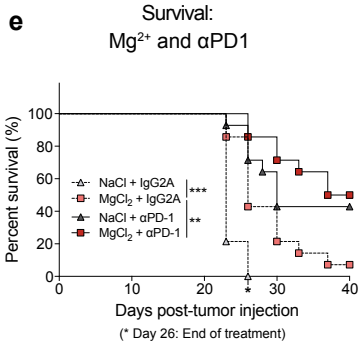
e
Survival: Mg2+ and αPD1
Percent survival (%)
NaCl + IgG2A
MgCl2 + IgG2A
NaCl + αPD-1
MgCl2 + αPD-1
***
**
*
Days post-tumor injection
(* Day 26: End of treatment)

Figure 1: Intratumoral magnesium administration improves adaptive anti-tumor immunity. (**a**) Schematic of experimental design (**b**) Tumor growth curves in non-immunized mice (n = 20) (*left panel*), and immunized mice (n = 19) (*right panel*). (**d**) Schematic of experimental design. (**e**) Tumor growth curves (n=13-14) and (**f**) host survival (n=13-14). Results were pooled from 2 independent experiments (**b**, **c**, **e**, **f**).

Data are presented as mean ± SEM, statistical significance was assessed by 2-way analysis of variance (ANOVA) with Bonferroni correction (**b**, **c** and **e**), and log-rank Mantel-Cox test (**f**). *p < 0.05, **p <0.01, *** p < 0.001, **** p < 0.0001.

Magnesium organismal distribution, and impact of magnesium depletion on memory $CD8^+$ T cells immunity

The magnitude of the effect that manipulating local Mg^{2+} levels had in our cancer immune-control model made us wonder how extracellular magnesium was distributed between anatomic sites. Organismal extracellular magnesium abundance was thus mapped both during steady state, and upon 2 weeks of dietary magnesium restriction (**Figure 2a**, *Experimental Scheme*). Intriguingly, extracellular magnesium distribution was heterogeneous between anatomic sites – with serum, lymph nodes and muscle being magnesium rich, while spleen, liver and, even more pronounced so, subcutaneous fatty tissue (notably the site where tumor cells were implanted in the above experiments) were naturally magnesium deplete (**Fig. 2b**). Short-term dietary magnesium restriction was efficiently depleting extracellular magnesium to approximately the low levels observed in subcutaneous fatty tissue (**Fig. 2b**). Depleting magnesium through two weeks of dietary intervention did not affect the general health status of mice (data not shown), and the body weight was comparable between cohorts (**Suppl. Figure 2a**). Complete blood counts revealed only small changes in platelet and erythrocyte numbers (**Suppl. Figure 2b**, *left panel*), as well as in hemoglobin levels and erythrocyte volumes (**Suppl. Figure 2b**, *middle panel*). Differential white blood cell counts showed no alterations in Mg^{2+} depleted animals (**Suppl. Figure 2b**, *right panel*). Further flow cytometric analyses indicated that Mg^{2+} depletion also had no relevant impact on $CD8^+$ T cells frequency; distribution of phenotypic subpopulations, and steady state expression of the activation marker CD69 (**Suppl. Figure 2c**-**e**). The percentage distribution of other lymphocyte subpopulations was likewise unaffected (**Suppl. Figure 2f**). To probe whether magnesium depletion had an effect on memory $CD8^+$ T cell mediated cytotoxicity, *in vivo* killing assays were performed (**Figure 2c**, *Experimental Scheme*). As target cells we used syngeneic splenocytes, pulsed with MHC class I-restricted $OVA_{257-264}$ peptide and dimly labelled with Cell Trace Violet. Non-pulsed splenocytes labelled brightly with Cell Trace Violet served as internal control. Antigen-specific clearance of target cells was lower in Mg^{2+} depleted hosts, with cytotoxicity partially rescued by co-injecting magnesium with target cells – pointing at a local effect of Mg^{2+} (**Figure 2d**). To further test the effect of magnesium on memory $CD8^+$ T cell function, a *Listeria monocytogenes* (LmOVA) intra-peritoneal (i.p.) infection model was used (**Figure 2e**, *Experimental Scheme*). Dietary depletion of Mg^{2+} reduced efficiency of memory $CD8^+$ T cell function also in this system and, further arguing for a local effect, spiking the i.p. bacterial inoculum with Mg^{2+} improved bacterial clearance (**Figure 2f**). In line with these immune control data, peritoneal abundance of Granzyme B was lower in magnesium depleted hosts and significantly rescued in mice receiving a Mg^{2+} spiked bacterial inoculum (**Figure 2g**). Of note, the innate cytokine IL-6 followed an inverse pattern, with markedly increased peritoneal and serum concentrations in mice less able to control infection (**Figure 2h** and

Suppl. Figure 2g, respectively) – plausibly reflecting increased innate inflammation due to a higher bacterial burden. To explore whether impaired $CD8^+$ T cell functionality was also reflected on an antigen-specific cellular level, surface expression of the degranulation marker CD107a and the activation maker CD69 were assessed on $CD8^+$ T cells isolated from the peritoneal cavity 20 h post-infection. Aligning with better immune control, expression of CD107a and CD69 was higher on $CD8^+$ T cells from Mg^{2+} competent than from Mg^{2+} depleted mice (**Figure 2i**,**j**). Spiking the bacterial inoculum with Mg^{2+} had a rescuing effect also for this readout (**Figure 2i**,**j**). The proportion of antigen-specific memory $CD8^+$ T cells in the peritoneal cavity was comparable between cohorts, suggesting that recruitment of antigen-specific cells to the site of infection was largely intact also in Mg^{2+} depleted mice (**Suppl. Figure 2h,i**).

In all these data established a previously unrecognized compartmentalization of extracellular Mg^{2+} between anatomic sites and demonstrated rapid Mg^{2+} depletion through dietary restriction. Depletion of Mg^{2+} specifically impaired memory $CD8^+$ T cell function, and add-back experiments suggested a direct, rapidly reversible effect of Mg^{2+} on memory $CD8^+$ T cells.

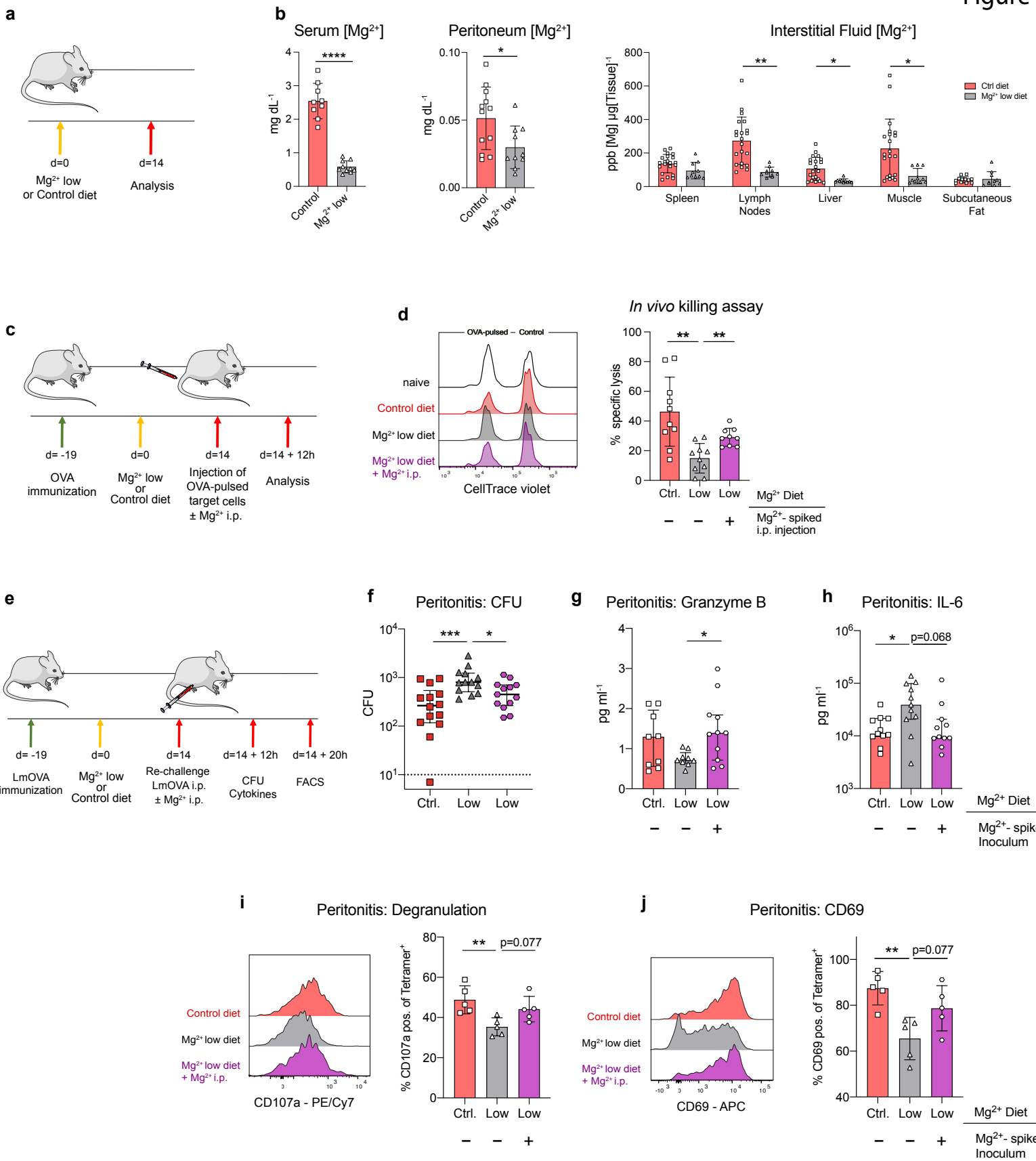
a
d=0
Mg2+ low or Control diet
d=14
Analysis
b
Serum [Mg2+]
mg dL-1
****
Control
Mg2+ low
Peritoneum [Mg2+]
*
Interstitial Fluid [Mg2+]
ppb [Mg] µg[Tissue]-1
**
*
*
Ctrl diet
Mg2+ low diet
Spleen
Lymph Nodes
Liver
Muscle
Subcutaneous Fat
c
d= -19
OVA immunization
d=0
Mg2+ low or Control diet
d=14
Injection of OVA-pulsed target cells ± Mg2+ i.p.
d=14 + 12h
Analysis
d
OVA-pulsed
Control
naive
Control diet
Mg2+ low diet
Mg2+ low diet + Mg2+ i.p.
CellTrace violet
In vivo killing assay
% specific lysis
**
**
Ctrl.
Low
Low
Mg2+ Diet
Mg2+- spiked i.p. injection
e
d= -19
LmOVA immunization
d=0
Mg2+ low or Control diet
d=14
Re-challenge LmOVA i.p. ± Mg2+ i.p.
d=14 + 12h
CFU Cytokines
d=14 + 20h
FACS
f
Peritonitis: CFU
CFU
***
*
g
Peritonitis: Granzyme B
pg ml-1
*
h
Peritonitis: IL-6
pg ml-1
*
p=0.068
Mg2+ Diet
Mg2+- spiked Inoculum
i
Peritonitis: Degranulation
Control diet
Mg2+ low diet
Mg2+ low diet + Mg2+ i.p.
CD107a - PE/Cy7
% CD107a pos. of Tetramer+
**
p=0.077
j
Peritonitis: CD69
Control diet
Mg2+ low diet
Mg2+ low diet + Mg2+ i.p.
CD69 - APC
% CD69 pos. of Tetramer+
**
p=0.077

Figure 2: Organismal magnesium depletion via dietary restriction impairs memory $CD8^+$ T cell mediated cytotoxicity. (**a**) Schematic of experimental design. Magnesium levels in serum (**b**, *left panel*), peritoneal lavage (**b**, *middle panel*), and interstitial fluids (**b**, *right panel*) from mice placed on Mg^{2+} reduced or matching control diet for 2 weeks. Results were pooled from 2-3 independent experiments. ppb = parts per billion (**c**) Schematic of experimental design. (**d**) Target cell clearance was evaluated in spleen. Representative flow cytogram (*left panel*), and summarized data from 2 independent experiments (*right*). (**e**) Schematic of experimental design. (**f**) Graph depicts bacterial burden in peritoneal lavage, data summarized from 3 independent experiments. Abundance of Granzyme B (**g**) and IL-6 (**h**) in corresponding peritoneal fluids. Expression of activation marker CD69 (**i**) and degranulation marker CD107a (**j**) on tetramer-positive memory $CD8^+$ T cells in the peritoneal. Representative flow cytogram (*left panel*), and summary data (*right panel*). Representative of n = 2 independent experiments.

Each symbol represents an individual mouse, bars indicate mean ± SD (**b, d, i, j**) or median ± IQR (**f, g, h**), dashed lines indicate detection limit and statistical significance was assessed by unpaired two-tailed Student's t test *left* and *middle panel* of (**b**) and (**d**), unpaired two-tailed Student's t test with Holm-Sidak corrected multiple comparison test (**b**, *right panel*) and one-way ANOVA with Sidak corrected multiple comparison test (**f**, **g**, **h**, **i**, **j**). *$p < 0.05$, **$p < 0.01$, *** $p < 0.001$, **** $p < 0.0001$.

Magnesium augments memory CD8$^+$ T cell function and moderately stabilizes LFA-1

Next, we aimed to directly probe for an effect of Mg^{2+} on memory CD8$^+$ T cell function, *in vitro*. Analysis of metabolic flux profiles revealed that glycolytic switching of human effector memory (EM) CD8$^+$ T cells, activated by injection of soluble anti-CD3/28 mAb, was blunted in absence of Mg^{2+}. This deficit was fully reverted when adding back Mg^{2+} just prior to activation (**Figure 3a**). By contrast, Mg^{2+} did not affect activation-induced upregulation of glycolysis in naïve CD8$^+$ T cells (**Figure 3b**). Notably, sensitivity of EM CD8$^+$ T cells for Mg^{2+} was lost in the context of supra-physiologic activation, achieved by injection of a secondary anti-antibody crosslinking the CD3/28 targeting mAbs (**Suppl. Figure 3a**). Naïve cells were unaffected by Mg^{2+} also in this experimental setting (**Suppl. Figure 3b**). Mg^{2+} thus directly impacted metabolic reprogramming of moderately activated memory but not naïve human CD8$^+$ T cells. The fact that the effect mediated by Mg^{2+} was overridden by supra-physiologic activation was suggestive of Mg^{2+} finetuning memory T cell activation. Next, we assessed the dose-effect of Mg^{2+} in EM CD8$^+$ T cells upon moderate TCR stimulation with plate-bound anti-CD3 mAb and soluble anti-CD28 mAb, staining for markers of: early and late activation (CD69 and CD25, respectively); metabolic reprogramming (CD71, CD98), and degranulation (CD107a). These experiments demonstrated a strict dose response, plateauing at 0.7 to 1.2 mM Mg^{2+}, i.e. in the range of reported Mg^{2+} plasma concentrations (**Figure 3c**) [31]. The stark difference in the capacity of memory CD8$^+$ T cells to upregulate these phenotypic markers in presence *vs.* absence of Mg^{2+} is summarized in **Figure 3d**. Also here, no Mg^{2+} related effect was observed for naïve CD8$^+$ T cells (**Suppl. Figure 3c**). Cytokine release (IFN-γ, TNF and IL-2) followed the pattern observed in the phenotypic studies, with decreased production under Mg^{2+} deplete conditions in EM cells (**Figure 3e**), yet no impact in naïve cells (**Suppl. Figure 3d**). Importantly, cell viability was not affected by lack of Mg^{2+} in culture media (**Suppl. Figure 3e**). The immediacy with which Mg^{2+} affected the activation threshold of EM CD8$^+$ T cells (**Figure 3a**), suggested to us a target (or targets) expressed on the cell surface, and one of the earliest events downstream from TCR engagement is signaling to integrins – which are essential for both basal and activation induced T cell migration. To understand if basal/random T cell motility was impacted by Mg^{2+}, under agarose migration experiments were performed. For practical reasons, human T cell blasts (PHA-blasts) were used for these experiments. In absence of extracellular Mg^{2+}, spontaneous migration (**Figure 3f**, *left panel*) and migration velocity (**Figure 3f**, *right panel*) were both significantly reduced in unstimulated T cell blasts. Inversely, activation-induced arrest of migration was incomplete in absence of extracellular Mg^{2+}, indicative of inefficient T cell activation (**Figure 3f**, *right panel*). Lending further supporting to the idea that Mg^{2+} was impacting a target (or targets) on the cell surface, clustering of activated T cell blasts was also appreciably reduced in absence of Mg^{2+} (**Figure 3g**).

Instructed by the detailed phenotypic and functional information on how magnesium was affecting key T cells features, we overlaid genes from gene ontology (GO) term lists in a Venn diagram, inputting the following terms: *metal binding ion* (parent term of *Mg^{2+} binding*); *immune synapse*; *leukocyte migration,* and *leukocyte adhesion*, together with a published list of proteins predominantly expressed by EM over naïve $CD8^+$ T cells [32]. This approach identified *ITGAL* (the gene encoding the Integrin Subunit Alpha L chain, CD11a) as candidate gene fulfilling the input criteria (**Figure 3h**). CD11a combines with ITGB2 (Integrin Subunit Beta 2 chain, CD18) to form leukocyte function-associated antigen (LFA-1). LFA-1 is an integrin-type cell adhesion molecule involved in T cell activation via immune synapse formation, as well as in leukocyte trafficking and extravasation [33]. Upon TCR stimulation, LFA-1 converts from a low affinity to a high-affinity state, a transformation coordinated by Mg^{2+} through binding to the metal-ion dependent adhesion site (MIDAS) on CD11a [34,35]. Cell surface expression was much lower on naïve than on EM $CD8^+$ T cells, expression on T cell blasts was highest (**Figure 3i**). Memory cell-selective Mg^{2+} dependency of metabolic reprogramming/activation, and Mg^{2+} dependency of migration and clustering of T cell blasts thus aligned with the selection of *ITGAL* through our GO-term integration approach.

The molecular conformation of LFA-1 can be probed for by flow cytometry, staining a neo-epitope exposed upon LFA-1 extension. Using this approach, we confirmed Mg^{2+} dependent extension of LFA-1 on moderately activated EM $CD8^+$ T cells (plate-bound anti-CD3 mAb, soluble anti-CD28 mAb), whereas the signal was weak for naïve cells (**Figure 3j**). When activated strongly, using beads loaded with anti-CD3/CD28 mAb at a proportion of 1:10, extension of LFA-1 was similar in presence and absence of Mg^{2+} (**Suppl. Figure 3f**). Also on T cell blasts, extension of LFA-1 was Mg^{2+} dependent unless the activation stimulus was strong (beads) (**Figure 3k**). Manganese (Mn^{2+}), like Mg^{2+}, binds to MIDAS motifs, with reported higher affinity [31]. Higher MIDAS affinity of Mn^{2+} was reflected also in our experiments through the fact that, while Mg^{2+} did not affect extension of LFA-1 in unstimulated T cells, Mn^{2+} did so (**Suppl. Figure 3g**). In its role as a high-affinity MIDAS ligand, Mn^{2+} was able to compensate for the lack of Mg^{2+} with respect to extension of LFA-1 in moderately activated T cell blasts – an effect again not seen when cells were activated strongly (**Figure 3k**). Further evidence for Mg^{2+} and Mn^{2+} exerting their effect via binding the MIDAS motif on CD11a came from inhibitor studies. Specifically, BIRT377, an allosteric inhibitor of LFA-1 – stabilizing its inactive, closed conformation – prevented activation-induced extension of the molecule in presence of both Mg^{2+} and Mn^{2+} (**Suppl. Figure 3h**). With a mimic of Mg^{2+} MIDAS-binding and an LFA-1 inhibitor (BIRT377) in hand, we revisited our experiments of Mg^{2+} dependent glycolytic switching, which confirmed that Mn^{2+} was able to compensate absence of Mg^{2+}, both in EM $CD8^+$ T cells (**Figure 3l**) and T cell blasts (**Suppl. Figure 3i**) – albeit not completely. Naïve $CD8^+$ T cells were not affected by Mn^{2+} to any significant extent (**Figure**

3m). Inversely, BIRT377 hindered both Mg^{2+} and Mn^{2+} from augmenting glycolytic switching of T cell blasts (**Figure 3o**). Importantly, in the context of supra-physiologic activation of T cell blast with PMA/ionomycin, neither Mg^{2+} restriction nor Mn^{2+} substitution altered glycolytic switching and no impact on steady-state glycolysis or oxidative phosphorylation were observed (**Suppl. Figure 3j**-**l**). In EM $CD8^+$ T cells, Mn^{2+} was also able to compensate, to some extent, for absence of Mg^{2+} with regard to upregulation of activation markers, and production of TNF (**Figure 3n**, and **Suppl. Figure 3m**), without negatively affecting cell viability (**Suppl. Figure 3n**). Likewise, when T cell blasts were activated moderately, Mn^{2+} partially rescued for lack of Mg^{2+} with respect to degranulation, upregulation of CD71 and production of TNF (**Suppl. Figure 3o**-**q**), in a BIRT377-sensitive manner (data not shown). By contrast, Mn^{2+} had no effect when T cell blasts were activated strongly (beads or PMA/ionomycin) (**Suppl. Figure 3o**-**q**).

Together these experiments pointed at a role for extracellular Mg^{2+} in tuning memory T cell function through binding to the MIDAS motif of LFA-1. Mn^{2+}, which binds the MIDAS motif with high affinity, more efficiently stabilized LFA-1 in its extended form. However, Mn^{2+} only partially substituted for Mg^{2+} with respect to glycolytic reprogramming and various immune functions, which suggested to us that moderate, rather than strong LFA-1 stabilization ideally supported EM $CD8^+$ T cell function [36]. Supraphysiologic activation of memory cells (activation beads; PMA/ionomycin) was overriding all proposed LFA-1 regulatory activity – also adding perspective to our *in vivo* data, where Mg^{2+} treated $CD8^+$ T cells where functionally superior, and expressed higher levels of activation markers, than NaCl exposed counterparts, a difference lost *ex vivo*, when restimulating with PMA and ionomycin.

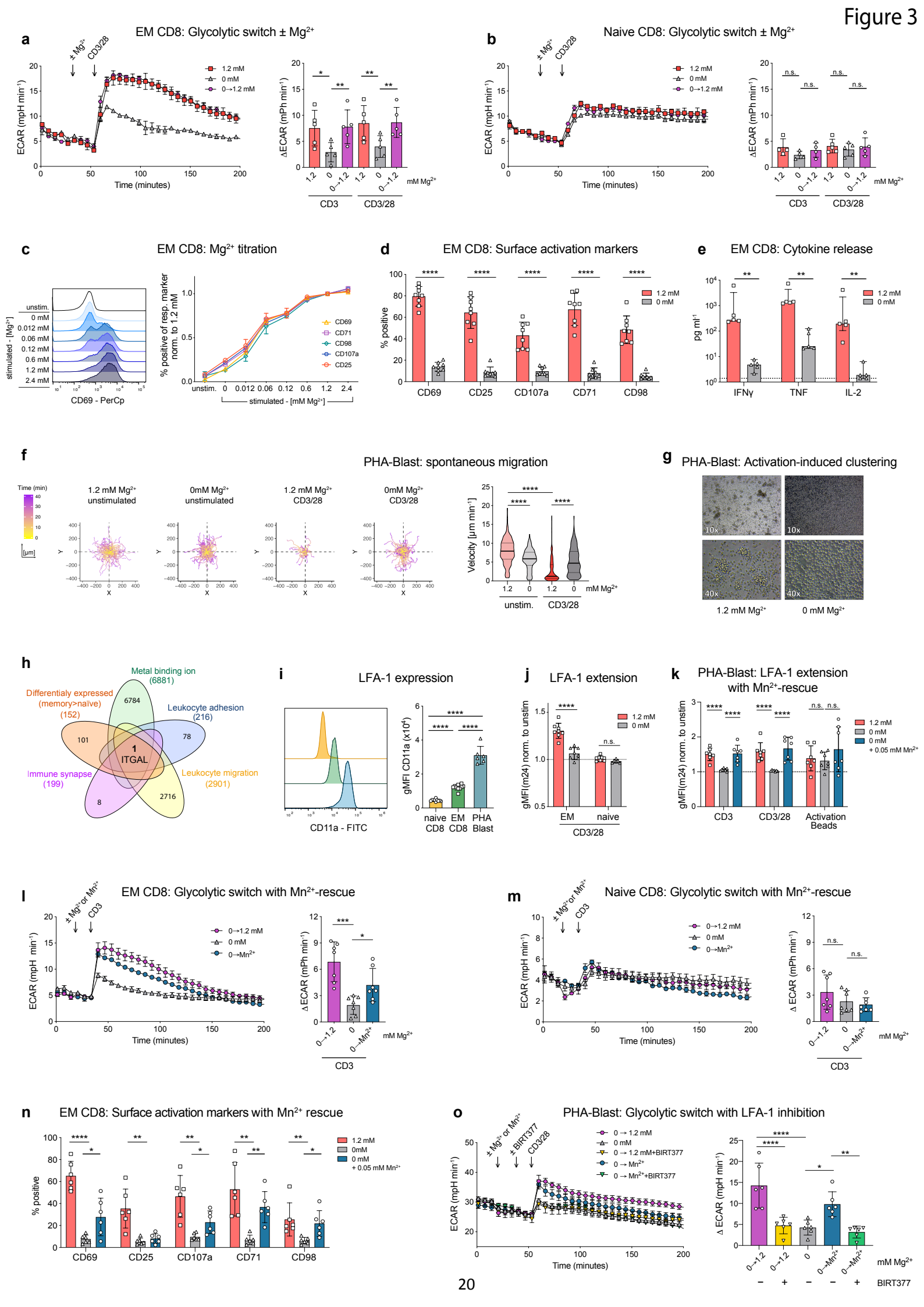
a
EM CD8: Glycolytic switch ± Mg2+
± Mg2+
CD3/28
1.2 mM
0 mM
0→1.2 mM
ECAR (mpH min-1)
Time (minutes)
ΔECAR (mPh min-1)
mM Mg2+
CD3
CD3/28
b
Naive CD8: Glycolytic switch ± Mg2+
n.s.
c
EM CD8: Mg2+ titration
unstim.
0 mM
0.012 mM
0.06 mM
0.12 mM
0.6 mM
1.2 mM
2.4 mM
stimulated - [Mg2+]
CD69 - PerCp
% positive of resp. marker norm. to 1.2 mM
CD69
CD71
CD98
CD107a
CD25
stimulated - [mM Mg2+]
d
EM CD8: Surface activation markers
% positive
e
EM CD8: Cytokine release
pg ml-1
IFNγ
TNF
IL-2
f
PHA-Blast: spontaneous migration
Time (min)
1.2 mM Mg2+ unstimulated
0mM Mg2+ unstimulated
1.2 mM Mg2+ CD3/28
0mM Mg2+ CD3/28
Velocity [µm min-1]
unstim.
CD3/28
g
PHA-Blast: Activation-induced clustering
10x
40x
1.2 mM Mg2+
0 mM Mg2+
h
Metal binding ion (6881)
Differentialy expressed (memory>naïve) (152)
Leukocyte adhesion (216)
Immune synapse (199)
Leukocyte migration (2901)
6784
101
78
1
ITGAL
8
2716
i
LFA-1 expression
CD11a - FITC
gMFI CD11a (x10⁴)
naive CD8
EM CD8
PHA Blast
j
LFA-1 extension
gMFI(m24) norm. to unstim
EM
naive
CD3/28
k
PHA-Blast: LFA-1 extension with Mn2+-rescue
0 mM + 0.05 mM Mn2+
CD3
CD3/28
Activation Beads
l
EM CD8: Glycolytic switch with Mn2+-rescue
± Mg2+ or Mn2+
CD3
0→Mn2+
m
Naive CD8: Glycolytic switch with Mn2+-rescue
n
EM CD8: Surface activation markers with Mn2+ rescue
0mM
o
PHA-Blast: Glycolytic switch with LFA-1 inhibition
± BIRT377
0 → 1.2 mM
0 mM
0 → 1.2 mM+BIRT377
0 → Mn2+
0 → Mn2+ +BIRT377
BIRT377

Figure 3: Extracellular magnesium promotes memory-specific activation via LFA-1. (**a**) and (**b**) Glycolytic switch of human $CD8^+$ T cell subsets upon injection of anti-CD3 antibody (anti-3) only, or combination of anti-CD3 and anti-CD28 antibody (anti-CD3/28 Ab), in medium containing either 1.2 mM Mg^{2+}, 0 mM Mg^{2+}, or medium which was reconstituted from 0 mM to 1.2 mM Mg^{2+} immediately prior to activation (0→1.2 mM Mg^{2+}). (**a**) Results for human effector memory (EM) and (**b**) for human naïve $CD8^+$ T cells. Traces of a representative experiment (*left panel*), and pooled data of >3 independent experiments (*right panel*). (**c**) Flow cytometric analysis of surface activation markers on human EM $CD8^+$ T cells activated at indicated Mg^{2+} concentrations. Representative flow cytogram of CD69 expression (*left panel*), and pooled data from 2 healthy donors (*right panel*). (**d**) Bar graph shows upregulation of surface activation markers on EM $CD8^+$ T cells. Pooled data from 5 independent experiments. (**e**) Abundance of inflammatory cytokines in corresponding cell culture supernatants. Dashed lines indicate detection limit. (**f**) Spontaneous migration of PHA-blasts confined on fibronectin-coated dishes under agarose ± 1.2 mM Mg^{2+}. Individual migration tracks plotted to common starting point over time (color coded) are depicted in *left panels*. Violin plot on the *right* shows median velocity of tracked cells (n=120-159). Representative of n=2 independent experiments. (**g**) Representative brightfield images of activation-induced clustering of PHA-blasts. (**h**) Venn diagram of GO Term lists and differentially expressed proteins between $CD8^+$ T cell subsets (memory > naïve). (**i**) Representative CD11a expression profile on human naïve and EM $CD8^+$ T cells as well human PHA-blasts as determined by flow cytometry (*left panel*) and summary bar graph (*right panel*). (**j**) Flow cytometry-based assessment of TCR activation-induced LFA-1 extension on human EM and naïve $CD8^+$ T cells. Pooled data of 4 independent experiments. (**k**) Analysis of LFA-1 extension on human PHA-Blast. Pooled data of 2 independent experiments. (**l**) and (**m**) Activation-induced glycolytic switch of human T cell subsets. Medium in all conditions was initially devoid of Mg^{2+} and, immediately prior to stimulation reconstituted to 1.2 mM Mg^{2+}, 0.05 mM Mn^{2+} – or kept at 0 mM Mg^{2+}, as indicated. (**l**) depicts results for EM and (**m**) for naïve $CD8^+$ T cells. One representative experiment (*left panel*) and pooled data from 3-4 independent experiments (*right panel*) are shown. (**n**) Activation induced glycolytic switch in PHA-blasts. Initial medium conditions as in (**l**), with addition of injection ± small-molecule CD11a inhibitor (BIRT377) prior to activation. Representative experiment (*left panel*) and quantification of summarized data from 2 independent experiments. (**o**) PMA/Ionomycin induced glycolytic switch in PHA-blast. *Left panel* illustrates representative experiment and *right panel* quantification of summarized data.

Each symbol represents an individual healthy donor, bars indicate mean ± SD *right panel* of (**a**, **b**, **l**, **m**, **n**, **o**) and (**c**, **d**, **i**, **j**, **k**) or median ± IQR (**e, f**). In representative metabolic flux analysis symbols indicate mean ±SEM *left panel* of (**a**, **k**, **l**, **m**). Statistical significance was assessed by repeated-measures one-

way ANOVA with Sidak's multiple comparison test (**a**, **b**, **l**, **m**) or one-way ANOVA with Sidak's multiple comparison test (**i**, **j**, **n**, **o**), unpaired two-tailed Student's test with Holm-Sidak multiple comparison test (**d**, **k**), Mann-Whitney test (**e**), and Kruskal-Wallis test with Dunn's multiple comparison test (**f**). *p < 0.05, **p <0.01, *** p < 0.001, **** p < 0.0001, n.s. = non-significant.

The Mg^{2+}–LFA-1 regulatory axis shapes cytotoxic T cell activity and immune synapse formation

To definitively probe the suggested Mg^{2+}–LFA-1 regulatory axis, experiments using LFA-1 deficient (LFA-$1^{-/-}$) cytotoxic T cells (CTLs) and LFA-$1^{-/-}$ Jurkat T cells were performed (**Suppl. Figure 4a**). First, we recapitulated metabolic analyses using LFA-$1^{-/-}$ CTLs. These experiments confirmed LFA-1 as the mediator through which Mg^{2+} exerted its effect on glycolytic switching (**Figure 4a**). 2-NBDG (glucose/nutrient) uptake assays – which were complemented with Mn^{2+} rescue and LFA-1 inhibition conditions (BIRT377) – also aligned with the metabolic flux studies (**Figure 4b**).

To further explore the breadth with which LFA-1 was affecting T cell activity, calcium (Ca^{2+}) flux experiments were performed. TCR stimulation mediates influx of Ca^{2+} into the cytosol, where it functions as a pivotal second messenger [37]. Depletion of extracellular Mg^{2+} decreased early, and fully aborted sustained influx of Ca^{2+} in wild type (WT) Jurkat T cells, a finding phenocopied independently of extracellular Mg^{2+} in LFA-$1^{-/-}$ Jurkat cells (**Figure 4c**). Sustained Ca^{2+} influx (indicated by black bar) is critically required for the assembly of multimolecular signaling complexes at immune synapses, thus shaping T cell activation [38,39]. As a proxy for early immune synapse-initiated signaling, we analyzed TCR ligation-induced tyrosine phosphorylation 2 min. post activation, using confocal microscopy. In LFA-$1^{-/-}$ Jurkat T cells, TCR induced tyrosine phosphorylation was markedly reduced, independently of extracellular Mg^{2+}. In WT Jurkat T cells, Mg^{2+} restriction had the same effect (**Figure 4d**). Similarly, in anti-CD3 mAb activated T cell blasts, phospho-tyrosine signaling was augmented by Mg^{2+} in a BIRT377-sensitive manner, and absence of Mg^{2+} was partially rescued by Mn^{2+} (**Suppl. Figure 4b**). Translocation of mitochondria towards the immune synapse supports influx of Ca^{2+} into the cytosol through local Ca^{2+} buffering, a process that requires signaling through LFA-1 [40]. To test whether Mg^{2+} was modulating this subcellular reorganization in CTLs, additional imaging studies were conducted. Focal accumulation of Granzyme B granules was used as a marker for the size of the immune synapse, with mitochondria expected to localize in close proximity of Granzyme B granules under optimal conditions. Indeed, in presence of extracellular Mg^{2+}, WT CTLs most efficiently recruited mitochondria and Granzyme B granules to the immune synapse (**Figure 4e**). LFA-1 further recruits, and amplifies, TCR-mediated ERK1/2 signaling at the immune synapse [41], and Mg^{2+}, and partially Mn^{2+}, increased also ERK1/2 activity in CTLs in an LFA-1 dependent manner (**Figure 4f**). Of note, Mg^{2+} and Mn^{2+} *per se* did not induce p-ERK1/2 in unstimulated T cells, nor did genetic deletion or LFA-1 negatively affect p-ERK1/2 signaling upon supra-physiologic activation (**Suppl. Figure 4c**). Engagement of ERK1/2 signaling and, in addition, also c-Jun-activity, through the LFA-1–Mg^{2+} regulatory axis was confirmed in human T cell blasts (**Suppl. Figure 4d**,**e**), as well as in primary human EM $CD8^+$ T cells (**Suppl. Figure 4f**). Together these functional and imaging analyses assigned Mg^{2+} an important role in orchestrating, through LFA-1, the architecture of the immune synapse and interlinked aspects of early TCR-initiated signaling activity.

With a clearer picture of the functional impact that the Mg^{2+}–LFA-1 system had in modulating early T cell activation, we moved on to investigate its impact on more downstream events in moderately (plate-bound anti-CD3 mAb, soluble anti-CD28 mAb) activated CTLs, namely upregulation of markers of activation (CD69) and degranulation (CD107a), as well as cytotoxic activity. These experiments pointed at lack of coordination between upregulation of CD69, degranulation and cytotoxic activity in LFA-$1^{-/-}$ cells. Specifically, CD69 and degranulation were induced similarly in activated LFA-1 competent and LFA-$1^{-/-}$ CTLs cells yet, as expected, only in LFA-1 competent cells they were modulated by Mg^{2+}, and partially also by Mn^{2+} (**Figure 4g**,**h**). Specific cytotoxic activity on the other hand – which is a highly coordinated process requiring polarized release of cytotoxic granules – was severely blunted in LFA-$1^{-/-}$ CTLs, while regulated via LFA-1 in a Mg^{2+} dependent, partially Mn^{2+} rescuable manner in LFA-1 competent counterparts (**Figure 4i**). This suggested that both, too much (Mn^{2+}) and too little (LFA-$1^{-/-}$) engagement of the Mg^{2+}–LFA-1 axis was associated with dysregulated immune function, plausibly due to uncoordinated immune synapse formation in both scenarios. Using OVA variant peptides (affinity for OT-I: G4 < H7 < R7), the importance of the Mg^{2+}–LFA-1 system in regulating specific target cell lysis was confirmed across a spectrum of TCR affinities, (**Figure 4j**). Only OVA, with its very high affinity for OT-I, did trigger limited lysis independently of Mg^{2+} and LFA-1 (**Figure 4j**). Aligning with this finding, cytotoxicity of murine CTLs was only regulated through Mg^{2+}–LFA-1 in low-dose PHA activated cells, but overridden at higher PHA doses (**Suppl. Fig. 4g**).

In all these results identified the Mg^{2+}–LFA-1 axis as an important regulatory system tuning the magnitude of TCR-triggered Ca^{2+} flux and signaling events; mitochondrial relocation towards the immune synapse, as well as the interlinked downstream lysis of target cells.

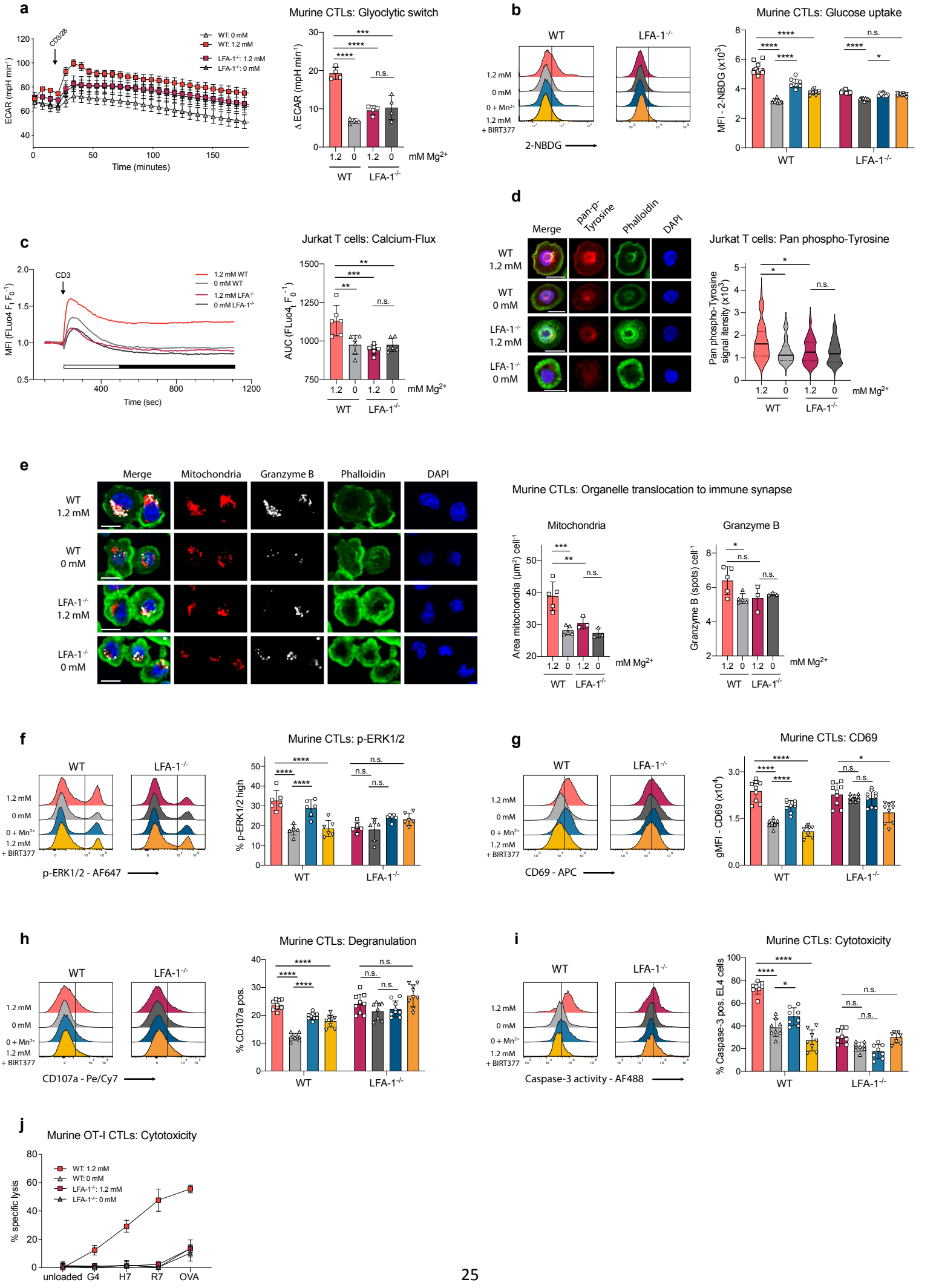
a
Murine CTLs: Glyoclytic switch
ECAR (mpH min-1)
Time (minutes)
CD3/28
WT: 0 mM
WT: 1.2 mM
LFA-1-/-: 1.2 mM
LFA-1-/-: 0 mM
Δ ECAR (mpH min-1)
mM Mg2+
WT
LFA-1-/-
b
Murine CTLs: Glucose uptake
WT
LFA-1-/-
1.2 mM
0 mM
0 + Mn2+
1.2 mM + BIRT377
2-NBDG
MFI - 2-NBDG (x10³)
c
Jurkat T cells: Calcium-Flux
CD3
1.2 mM WT
0 mM WT
1.2 mM LFA-1-/-
0 mM LFA-1-/-
MFI (FLuo4 Ft Fo-1)
Time (sec)
AUC (FLuo4 Ft Fo-1)
d
Merge
pan-p-Tyrosine
Phalloidin
DAPI
Jurkat T cells: Pan phospho-Tyrosine
Pan phospho-Tyrosine signal itensity (x10³)
e
Merge
Mitochondria
Granzyme B
Phalloidin
DAPI
Murine CTLs: Organelle translocation to immune synapse
Mitochondria
Granzyme B
Area mitochondria (μm²) cell-1
Granzyme B (spots) cell-1
f
Murine CTLs: p-ERK1/2
p-ERK1/2 - AF647
% p-ERK1/2 high
g
Murine CTLs: CD69
CD69 - APC
gMFI - CD69 (x10⁴)
h
Murine CTLs: Degranulation
CD107a - Pe/Cy7
% CD107a pos.
i
Murine CTLs: Cytotoxicity
Caspase-3 activity - AF488
% Caspase-3 pos. EL4 cells
j
Murine OT-I CTLs: Cytotoxicity
WT: 1.2 mM
WT: 0 mM
LFA-1-/-: 1.2 mM
LFA-1-/-: 0 mM
% specific lysis
unloaded
G4
H7
R7
OVA

Figure 4: Magnesium regulates LFA-1 mediated T cell activation and cytotoxicity within physiologic-range. (**a**) Glycolytic switch upon activation of murine WT and LFA-$1^{-/-}$ CTLs. Representative experiment (*left panel*), quantification of summarized data (*right panel*) with n=4 mice. (**b**) Glucose uptake by activated murine WT and LFA-$1^{-/-}$ CTLs. Representative flow cytogram profile (*left panel*) and summary graph of n=3 mice with 3 technical replicates each (*right panel*). (**c**) TCR-stimulation induced calcium flux in WT and LFA-$1^{-/-}$ Jurkat T cells. Representative trace (*left panel*), and quantification of area under the curve (AUC) of 3 independent experiments in duplicates (*right panel*). (**d**) *Left panel*, representative immunofluorescent images of WT and LFA-$1^{-/-}$ Jurkat T cells stimulated for 2 min on anti-CD3 Ab coated coverslip. Images are displayed as confocal projections of 3D stacks. Scale bars indicate 10 µm. *Right panel*, quantitative analysis of fluorescent signal intensity (n = 62-71 cells/condition, pooled from 2 different field of views). (**e**) *Left panel*, representative immunofluorescent images of WT and LFA-$1^{-/-}$ murine CTLs stimulated for 5 min on anti-CD3 Ab coated coverslip. Images are *Z*-projections of 11 stacks within closest proximity to anti-CD3 Ab coated coverslip. Scale bars indicate 10 µm. Right, quantitative analysis of fluorescent signal abundance. Each symbol represents an individual field of view. (**f** – **h**) Representative histograms (*left panel*) and quantified results of n=3 mice with 3 technical replicates each (*right panel*). (**f**)Phosphorylation of ERK1/2, (**g**) surface expression of CD69 and (**h**) CD107a on murine WT and LFA-$1^{-/-}$ CTLs. (**i**) Caspase-3 activity in EL4 target cells after co-culture with murine WT and LFA-$1^{-/-}$ CTLs. Representative histogram shows Caspase-3 activity in EL4 cells assed by flow cytometry (*left panel*), results are quantified of n=3 mice with 3 technical replicates each (*right panel*). (**j**) Cytotoxicity assay using WT and LFA-$1^{-/-}$ OT-I CTLs, co-cultured with cognate antigen-pulsed luciferase-expressing EL4 target cells. (n=4 mice).

Data are presented as mean ± SD *right panel* of (**a** - **c**) and (**e** - **j**) or median ± IQR (**d**). In representative metabolic flux traces, *left panel* of (**a**), symbols indicate mean ±SEM and traces of representative calcium flux, *left panel* of (**c**), indicate mean of duplicate wells. Statistical significance was assessed by one-way ANOVA with Sidak's multiple comparison test (**a – c**) and (**e – i**) as well Kruskal-Wallis test with Dunn's multiple comparisons test was applied for (**d**), respectively. *$p < 0.05$, **$p < 0.01$, *** $p < 0.001$, **** $p < 0.0001$, n.s. = non-significant.

Immune synapse formation of expanded tumor-specific T cells is regulated via the Mg^{2+}–LFA-1 axis

Autologous tumor-specific T cells, expanded *in vitro* using rapid expansion protocols (REP), are holding great promise for treating cancer [42]. The NY-ESO-1 antigen is considered a promising target for immunotherapy as it is expressed by numerous malignancies [43]. LFA-1 surface expression on human NY-ESO-1-specific REP T cells was found to be as high as on T cell blasts (PHA blasts) (**Figure 5a**), making them a relevant model to study potential translational usefulness of the Mg^{2+}–LFA-1 modulatory system. Mg^{2+} dependency of ERK1/2 and c-Jun activity, as well degranulation and cytotoxicity, were recapitulated in NY-ESO-1-specific REP T cells co-cultured with antigen pulsed tumor target cells (**Figure 5b**-**e**). Mn^{2+} overcompensated for Mg^{2+} depletion with respect to ERK1/2 and c-Jun activity, while only partially rescuing Mg^{2+} depletion as related to cytotoxicity – again underscoring the importance of moderate, i.e. Mg^{2+} mediated, LFA-1 stabilization to optimally support this biologically complex endpoint. As expected, BIRT377 blocked target cell induced T cell activation (**Figure 5b**-**e**). Peptide titration experiments indicated that dependency of REP T cells on Mg^{2+} for target cell killing was more pronounced with low concentrations of cognate peptide expressed on tumor cells (**Suppl. Figure 5a**). Encouraged by these functional data we went on to explore how they related with immune synapse formation. To do so, REP T cells were incubated for 10 min with target cells either pulsed with cognate peptide (9c) or left unpulsed, and cell-cell conjugates were analyzed by confocal microscopy. Visually, and in a quantifiable manner, these experiments identified early antigen-specific, Mg^{2+} dependent and Mn^{2+} rescuable, LFA-1 activation at sites of close physical interaction between REP T cells and tumor targets (**Figure 5f***, upper panel* and *lower left panel*). The Mg^{2+} requirement for LFA-1 activation previously observed in human memory T cells and Jurkat T cells activated with antibodies (**Figure 3j**,**3k**) was thus replicating in a biologically relevant cell-cell interaction system. Phospho-tyrosine signal intensity at REP T cell–target cell interaction sites also mirrored LFA-1 extension across all conditions (**Figure 5f***, upper panel and lower right panel*), again aligning with data obtained previously (**Figure 4d** – Jurkat T cells and **Suppl. Figure 4b** – T cell blasts). Maturation of the immune synapse is characterized by centrosome polarization and focused delivery of cytolytic granules, and indeed – after 35 min of REP T cells–tumor target cell co-incubation – the Mg^{2+}–LFA-1 axis contributed also to both these later stage events (**Figure 5g**). Together, these data expanded relevance of the Mg^{2+}–LFA-1 system to a biologically and clinically relevant system and added insight into its role in supporting formation of the immune synapse.

Figure 5

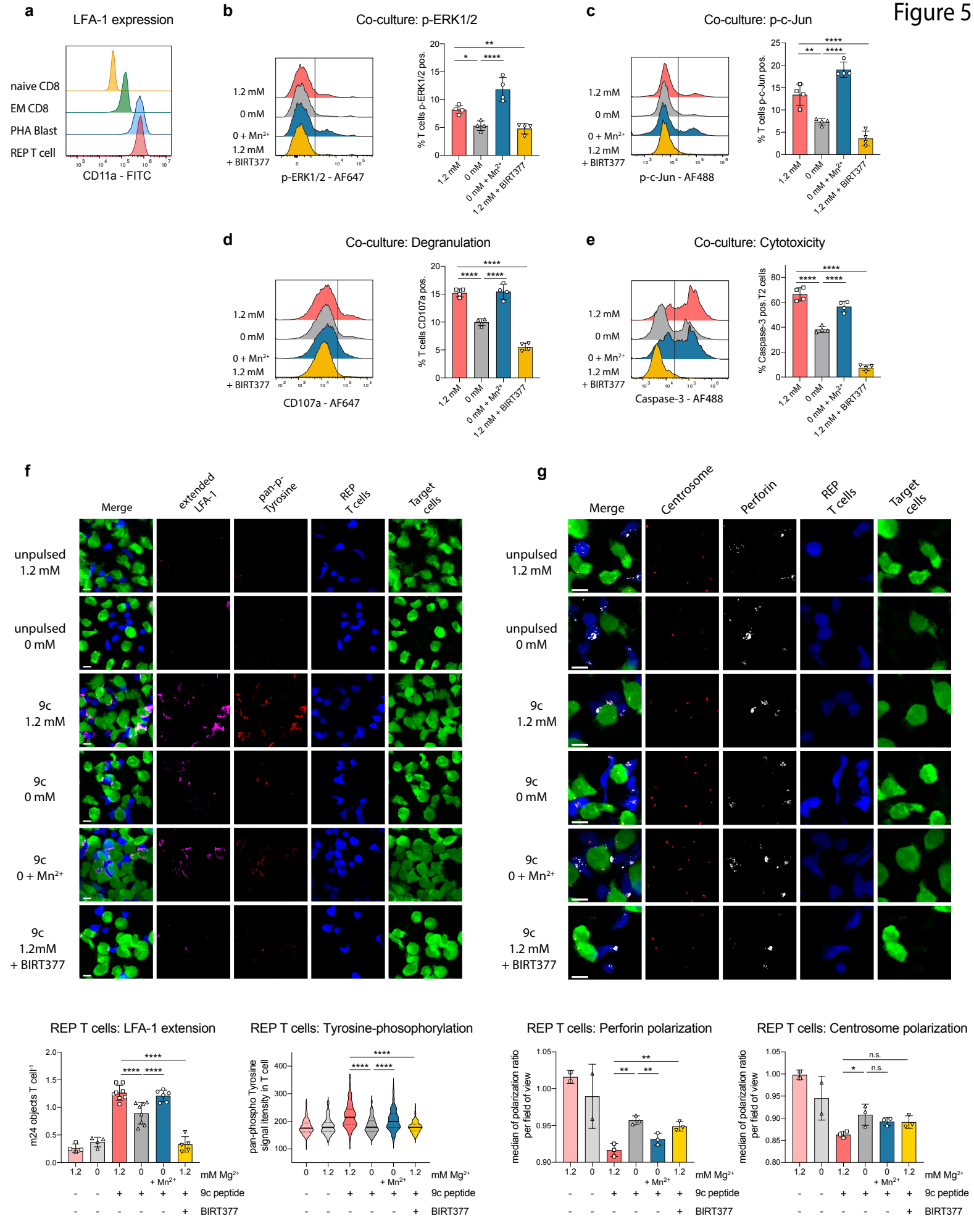
a
LFA-1 expression
naive CD8
EM CD8
PHA Blast
REP T cell
CD11a - FITC
b
Co-culture: p-ERK1/2
1.2 mM
0 mM
0 + Mn2+
1.2 mM + BIRT377
p-ERK1/2 - AF647
% T cells p-ERK1/2 pos.
c
Co-culture: p-c-Jun
p-c-Jun - AF488
% T cells p-c-Jun pos.
d
Co-culture: Degranulation
CD107a - AF647
% T cells CD107a pos.
e
Co-culture: Cytotoxicity
Caspase-3 - AF488
% Caspase-3 pos.T2 cells
f
Merge
extended LFA-1
pan-p-Tyrosine
REP T cells
Target cells
unpulsed 1.2 mM
unpulsed 0 mM
9c 1.2 mM
9c 0 mM
9c 0 + Mn2+
9c 1.2mM + BIRT377
g
Merge
Centrosome
Perforin
REP T cells
Target cells
unpulsed 1.2 mM
unpulsed 0 mM
9c 1.2 mM
9c 0 mM
9c 0 + Mn2+
9c 1.2 mM + BIRT377
REP T cells: LFA-1 extension
m24 objects T cell-1
REP T cells: Tyrosine-phosophorylation
pan-phospho Tyrosine signal itensity in T cell
REP T cells: Perforin polarization
median of polarization ratio per field of view
REP T cells: Centrosome polarization
median of polarization ratio per field of view
mM Mg2+
+ Mn2+
9c peptide
BIRT377

Figure 5: Magnesium-LFA-1 axis regulates immune synapse formation of tumor-specific human T cells. (**a**) Representative histogram of CD11a expression on human naïve and EM $CD8^+$ T cells, PHA-blasts and NY-ESO-1-specific REP T cells. (**b** -**e**) Representative histograms (*left panel*), quantified results of n=1 healthy donor with 4 technical replicates (*right panel*). Phosphorylation of ERK1/2 (**b**) and c-Jun (**c**) in human REP T cells as well (**d**) surface expression of CD107a on REP T cells after incubating with cognate-peptide pulsed T2 target cells. (**e**) Caspase-3 activity in T2 target cells, after co-culturing with REP T cells. (**f**) *Top panel*, representative confocal projections of REP T cells mixed with T2 target cells labeled for extended LFA-1 and pan-tyrosine phosphorylation. Scale bars indicate 10 µm. *Bottom-left panel*, quantitation of extended LFA-1 within confocal 3D stacks (symbol represents an individual field of view). *Bottom-right panel*, quantitation of median fluorescent intensity of tyrosine phosphorylation in REP T cells (n = 203 - 344 cells per condition, pooled from n= 1 - 2 field of views). (**g**) *Top panel*, representative confocal projections of REP T cells mixed with T2 target cells. Cells were labeled for γ-tubulin (centrosome) and perforin. *Bottom left panel*, quantitation of perforin and centrosome (*bottom right*) polarization (symbol represents an individual field of view). Data are presented as mean ± SD, except for *bottom right panel* of (**f**) where data is presented as median ± IQR. Statistical significance was assessed by one-way ANOVA with Sidak's multiple comparison test (**b**, **c**, **d**, **e**) and *bottom left panel* of (**f**, **g**) as well *bottom right panel* of (**g**). Kruskal-Wallis test with Dunn's multiple comparison test was used for *bottom right panel* of (**f**). *$p < 0.05$, **$p < 0.01$, *** $p < 0.001$, **** $p < 0.0001$, n.s. = non-significant

Mg^{2+} availability shapes anti-tumor activity of CAR T cells, *in vitro* and *in vivo*

In patients with hematologic malignancies, chimeric antigen receptor (CAR) T cells have demonstrated remarkable efficiency. However, not all patients respond to CAR T cell therapy, and in solid cancers, CAR T cells are largely ineffective – highlighting the need for improvement. To explore the potential clinical relevance of manipulating Mg^{2+} levels in the CAR T cell context, human CAR T cells specific for prostate-specific membrane antigen (PSMA) were used [44]. When activated with soluble anti-CD3/CD28 mAb, these CAR T cells depended on Mg^{2+} both with respect to glycolytic reprogramming and phenotypic changes (**Figure 6a**,**b**). Having confirmed Mg^{2+} dependency also of CAR T cell activation, we went on to assess their cytotoxicity. Time-lapse killing assays demonstrated that Mg^{2+} restriction severely blunted specific killing of target cells (**Figure 6c**). Concomitantly, release of IFN-γ by CAR T cells was also reduced in Mg^{2+} deplete conditions (**Figure 6d**). To probe whether dietary restriction, reducing systemic and, by trend, also intratumoral Mg^{2+} abundance (**Figure 2b**, and **Suppl. Figure 6a**), might affect CAR T cell mediated cytotoxicity, tumor rejection experiments were performed (**Figure 6e**, *Experimental Scheme*). Indeed, dietary Mg^{2+} restriction was sufficient to negatively impacted CAR T cell-mediated tumor-rejection, *in vivo*. Food intake was comparable between the cohorts, yet tumor-bearing mice fed a Mg^{2+} depleted diet had a lower body weight by day 25 of the experiment (**Suppl. Figure 6b**,**c**), indicative of a more catabolic state. While the impact of mild intratumoral Mg^{2+} depletion was less pronounced than the opposite experiment where Mg^{2+} was injected into the tumor (**Figure 1a**-**e**), the effect was still clear. This prompted us to retrospectively assess a cohort of 100 patients with refractory B cell lymphoma who were treated with CD19 directed CAR T cells (axicabtagen ciloleucel – Yescarta®) (**Suppl. Figure 6d**, *Study Diagram*, and **Suppl. Figure 6e**, *Baseline Characteristics*). Patients fell into three strata according to the number of Mg^{2+} measurements < 1.6 mg dl^{-1}, between days -5 and $^{+}3$ of treatment (**Figure 6g**, and **Suppl. Figure 6f**). Although the number of patients with severe hypomagnesemia was low, median progression-free survival for these patients was only 1 month, as compared to 6.5 months in patients with normal serum Mg^{2+} levels (**Figure 6h**), and median overall survival was 1 month *vs.* 8 months (**Suppl. Figure 6g**). In line with these data, all patients with grade II hypomagnesemia died, whereas the disease progression rate was 52.5% for patients with normal serum Mg^{2+} (**Figure 6i**). While this retrospective analysis has many limitations, in the context of the experimental CAR T cell data the findings aligned with the concept that Mg^{2+}, through physiologic LFA-1 stabilization, may contribute to clinical efficacy of CAR T cells in human patients

.

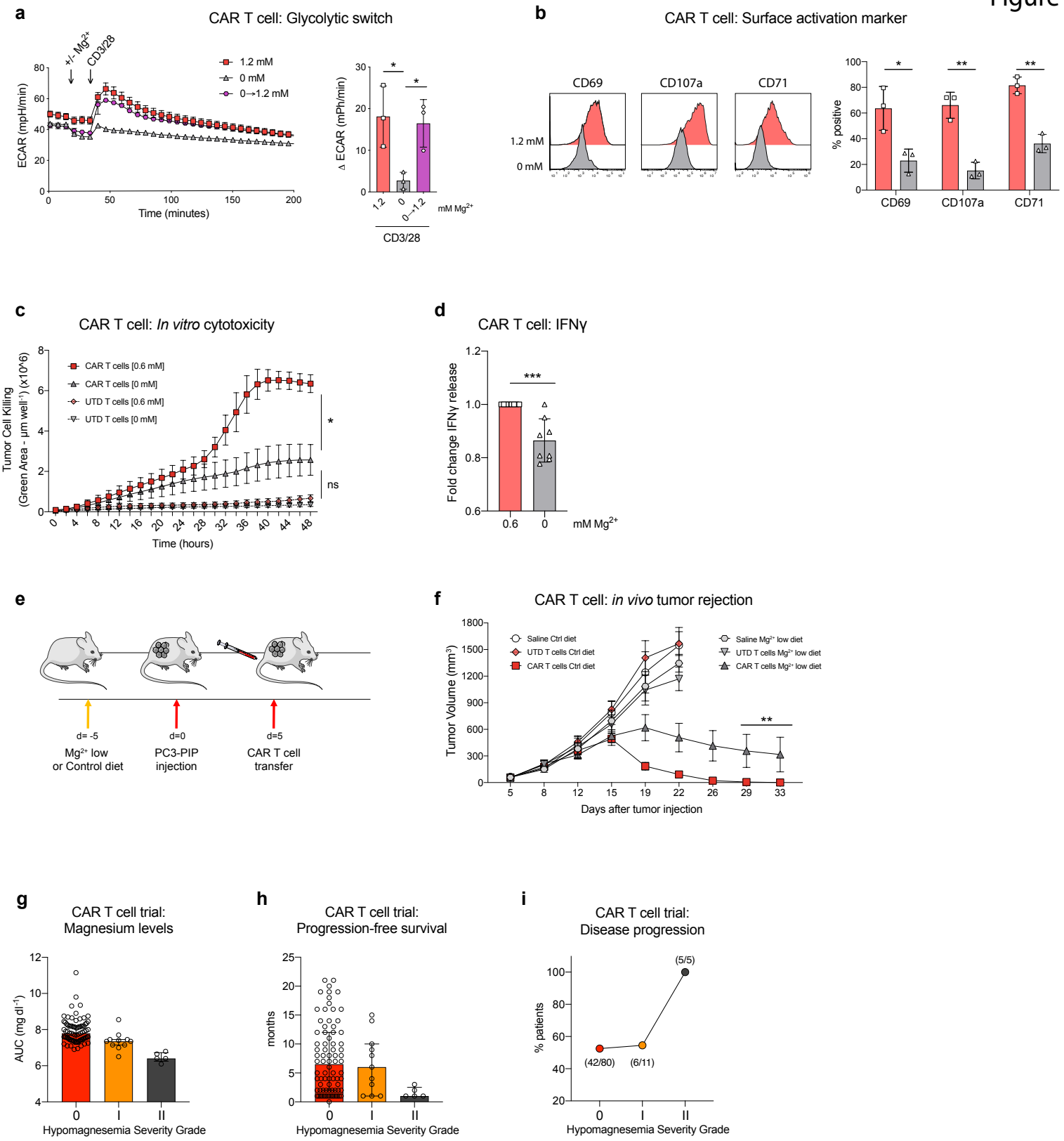
a
CAR T cell: Glycolytic switch
+/- Mg2+
CD3/28
1.2 mM
0 mM
0→1.2 mM
ECAR (mpH/min)
Time (minutes)
Δ ECAR (mPh/min)
mM Mg2+
CD3/28
b
CAR T cell: Surface activation marker
CD69
CD107a
CD71
1.2 mM
0 mM
% positive
c
CAR T cell: In vitro cytotoxicity
CAR T cells [0.6 mM]
CAR T cells [0 mM]
UTD T cells [0.6 mM]
UTD T cells [0 mM]
Tumor Cell Killing (Green Area - µm well-1) (x10^6)
Time (hours)
ns
d
CAR T cell: IFNγ
Fold change IFNγ release
mM Mg2+
e
d= -5
Mg2+ low or Control diet
d=0
PC3-PIP injection
d=5
CAR T cell transfer
f
CAR T cell: in vivo tumor rejection
Saline Ctrl diet
UTD T cells Ctrl diet
CAR T cells Ctrl diet
Saline Mg2+ low diet
UTD T cells Mg2+ low diet
CAR T cells Mg2+ low diet
Tumor Volume (mm3)
Days after tumor injection
g
CAR T cell trial: Magnesium levels
AUC (mg dl-1)
Hypomagnesemia Severity Grade
h
CAR T cell trial: Progression-free survival
months
Hypomagnesemia Severity Grade
i
CAR T cell trial: Disease progression
% patients
(42/80)
(6/11)
(5/5)
Hypomagnesemia Severity Grade

Figure 6: Extracellular magnesium shapes CAR T cell functionality *in vitro* and *in vivo.* (**a**) Activation-induced glycolytic switch of human CAR T cells. Representative experiment (*left panel*), quantification of summarized data (*right panel*) with n=3 healthy donors. (**b**) *Left panel*, representative histograms of surface activation markers on CAR T cells. *Right panel* shows quantitation of respective stainings with n=3 healthy donors. (**c**) Cytotoxicity assay with anti-PSMA CAR T cells and UTD T cells co-cultured with $PSMA^+$ PC3-PIP cell line. Pooled results of n=6 healthy donors from 2 independent experiments are shown. (**d**) Abundance of IFNγ in cell culture supernatants corresponding to conditions depicted in (**c**) (n=8, 3 independent experiments). (**e**) Schematic of experimental design. (**f**) Tumor growth curves. Representative of n=2 independent experiments with n = 6 mice per group. (**g**) Comparison of serum magnesium levels among three grades of hypomagnesemia severity grades. Values are presented as AUC over 5 initial measurements. Each symbol represents individual patient. (**h**) Progression-free survival of patients allocated to different hypomagnesemia severity grading. Each symbol represents individual patient. (**i**) Comparison of disease progression, including death, across different levels of hypomagnesemia. Numbers in parentheses represent proportion of patients with disease progression in respective group.

Data are presented as mean ± SD *right panel* of (**a**) and (**b**, **d**), mean ± SEM (**c**, **f**) or median ± IQR (**g**, **h**). In representative metabolic flux analysis symbols indicate mean ±SEM *left panel* of (**a**). Statistical significance was assessed by one-way ANOVA with Sidak's multiple comparison test (**a**), unpaired two-tailed Student's t test with Holm-Sidak corrected multiple comparison test (**b**), unpaired student's T test (**d**) or two-way ANOVA with post hoc Tukey test (**f**). *$p < 0.05$, **$p < 0.01$, *** $p < 0.001$, **** $p < 0.0001$, n.s. = non-significant.

DISCUSSION

Three key findings emerged from this study – immunologic, physiologic and molecular in nature, respectively. The most important immunologic observation was that extracellular Mg^{2+} functioned as a powerful modulator of T cell cytotoxicity. Compartmentalized distribution of extracellular Mg^{2+}, with existence of naturally Mg^{2+} deplete tissue sites, was a surprising physiologic feature of this important ion. On a molecular level, moderate LFA-1 activation through Mg^{2+} was critical for the delivery of the right amount of LFA-1 outside-in signaling to support immune synapse formation and thus targeted, antigen-specific cytotoxicity.

The presence of other major ions in the extracellular space, such as potassium (K^+) and sodium (Na^+) has previously been implicated in direct modulation of T cell function. Specifically, intratumoral K^+ – released by necrotic cancer cells – has been described as an important modulator of anti-tumor T cell responses through suppression of TCR-driven Akt–mTOR phosphorylation, and thus cytotoxic effector functions [45]. With regard to Na^+, high local concentrations have been shown to drive phosphorylation of p38 MAPK, thereby initiating a cascade of events resulting in increased Th17 T cell polarization [46].

Here, extracellular Mg^{2+} emerged as a previously unrecognized immune modulator, affecting the activation-threshold of antigen specific memory $CD8^+$ T cells. Given the compartmentalized distribution of Mg^{2+} in healthy mice, this plausibly creates tissue-specific differences in the TCR signal strength required to activate memory $CD8^+$ T cells engaging in immune surveillance of Mg^{2+} high *vs.* Mg^{2+} low tissues. It will be interesting to explore whether compartment-specific effects on the $CD8^+$ T cell activation threshold affect infection control, cancer immune control – but also the occurrence of autoimmunity.

Improving conventional cancer therapy by manipulating nutrient availability through dietary intervention is a field of growing interest [47]. For example, experimental data suggest beneficial effects of repetitive fasting cycles in mice, the rational being to target high metabolic requirements of cancer cells [48]. When aiming to translate such deprivation strategies to clinical medicine these need, however, to be carefully balanced against the danger of imposing nutrient deficiencies that may negatively impact on host immunity. Indeed, only two weeks of dietary depletion of Mg^{2+} were sufficient to affect both tumor and infection immune control in mice, and low serum Mg^{2+} levels were associated with an unfavorable outcome in CAR T cell treated human patients. Experimental data also support the idea of adding, rather than depleting, nutrients in order to enhance the response to conventional cancer therapies. Histidine supplementation, for example, has been shown to increase responsiveness to methotrexate in a mouse model of leukemia [49], and supplementation of creatine was found to improve T cell anti-tumor immunity in multiple mouse tumor models [50]. Our data add to the discussion of such strategies by showing that Mg^{2+} sufficient animals compartmentalized availability of this ion

in the extracellular space. While not formally tested in this study, it is unlikely that Mg^{2+} high diet would dramatically alter this organismal distribution. This could apply also to other nutrients/dietary additions that therefore might not necessarily reach target concentrations in a given tissue of interest simply through increased dietary intake. Despite the complexity of compartmentalization, our findings do suggest that studying the role of treating and/or preventing magnesium deficiency in clinical cancer medicine will be of relevance. All the more so, since hypomagnesemia is the most underdiagnosed electrolyte deficiency [51], and platin-based chemotherapeutics can induce severe hypomagnesemia [52,53].

The key molecular insight from our experiments was that LFA-1 signaling, albeit critically important, had to be moderate – as was achieved by Mg^{2+} binding – in order to ideally prime specific cytotoxicity and optimal immune synapse formation. Perhaps not surprisingly, also in light of our date, complete pharmacological inhibition of LFA-1 in the context of autoimmunity has failed due to overly severe immunosuppression [54]. Since LFA-1 activation *in moderation* was critical in our experimental systems, it is more interesting perhaps to note that robustly stabilizing LFA-1 in its extended form, using a mAb, and transferring T cells expressing constitutively extended LFA-1, both severely impaired T cell responses *in vitro* and *in vivo* [55,56]. Our observations are providing context to these findings, as Mn^{2+} was also negatively impacting critical immunologic endpoints, such immune-synapse formation and target cell lysis, despite the fact that Mn^{2+} outperformed Mg^{2+} with regard to stabilizing LFA-1. The decline in the capacity of Mn^{2+} to replace Mg^{2+} was becoming ever more apparent with increasing biological complexity of the studied endpoint. This underscored the importance of the requirement for *moderate* LFA-1 stabilization to appropriately activate $CD8^+$ T cells and thus achieve an optimal functional outcome.

The striking effect that intratumoral $MgCl_2$ injections had on T cell-mediated tumor control may instruct translational efforts aiming to explore usefulness of increasing Mg^{2+} abundance in cancer tissues in clinical medicine. Correcting organismal Mg^{2+} deficiency may represent one therapeutic pillar, yet judging from our CAR T cell data this will only partially tap the potential that may lie in targeting Mg^{2+} directly into cancer tissue. Superficial cancers, such as (often) melanoma or breast cancer, could be simply injected with Mg^{2+}, and specific pharmacological formulations might be used to slow diffusion of Mg^{2+} into adjacent tissues. More sophisticated strategies might include developing T cell-linked synthetic nanoparticles specifically accumulating Mg^{2+} at the immune synapse [57], or coupling of Mg^{2+} loaded liposomes to immune checkpoint inhibitors. This strategy seems all the more appealing since more than 25% of colorectal cancer-infiltrating $CD8^+$ T cells co-expressed both PD1 and LFA-1 in an analysis available through the iSTAR data base [58].

In conclusion, our data identified extracellular Mg^{2+} as an immunomodulator, specifically augmenting T cell activation in the range of low to moderate TCR stimulation via its moderate LFA-1 stabilizing properties. Through this role, Mg^{2+} defined the threshold of T cell activation in a subset (defined by high *vs.* low cell surface expression of LFA-1), and tissue specific manner (compartmentalized abundance). On a molecular level, Mg^{2+} enabled assembly of multimolecular signaling complexes; Ca^{2+} flux; translocation of mitochondria, and metabolic reprogramming in $CD8^+$ T cells – jointly enabling efficient and specific cytotoxic activity. Conceptually, studying the molecular physiology of signaling molecules may help uncover therapeutic windows that could be missed in less nuanced loss- and gain-of-function screening approaches.

MATERIALS AND METHODS

Cell culture media

For the culture of primary human $CD8^+$ T cells, PHA-induced T cell blasts, Jurkat T cells, PC3-PIP and T2 cells, RPMI-1640 medium (Invitrogen) was supplemented with heat-inactivated 10% fetal calf serum (HI FCS, Gibco), 50 U mL^{-1} penicillin (Invitrogen) and 50 µg mL^{-1} streptomycin (Invitrogen). Human REP T cells were expanded in AIM V medium (Thermo Fisher) mixed 1:1 with RPMI-1640 (Invitrogen) supplemented with 10% human HI AB serum, 50 U mL^{-1} penicillin (Invitrogen) and 50 µg mL^{-1} streptomycin, 1 mM pyruvate (Gibco), 1% MEM Non-Essential Amino Acids (Gibco), 1% GlutaMAX (Gibco) and 3,000 U mL^{-1} human recombinant IL-2 (Proleukin, Novartis). Murine T cells und EL4 cells were kept in RPMI-1640 medium containing 10% HI FCS, 100 U mL^{-1} penicillin, 100 µg streptomycin, 0.29 mg mL^{-1} L-glutamine, 50 µM 2-Mercaptoethanol (Invitrogen). 293T human embryonic kidney (HEK-293T) were cultured in RPMI-1640 supplemented with 10% HI FCS, 2 mmol l-glutamine, 100 µg mL^{-1} penicillin and 100 U mL^{-1} streptomycin (all purchased from Invitrogen). MC38-OVA cells were maintained in RPMI-1640-Glutamax medium supplemented with 10% FCS, 50 U mL^{-1} penicillin and 50 µg mL^{-1} streptomycin, 1 mM sodium pyruvate, 50 µM 2-Mercaptoethanol and under geneticin selection (0.4 mg mL^{-1} G418). All reagents were purchased from Gibco. Magnesium-free medium was made in-house, using double distilled water supplemented according to manufacturer's instruction with RPMI-1640 amino acid solution (Sigma Aldrich), RPMI-1640 vitamin solution (Sigma Aldrich), 1% GlutaMAX (Gibco), 25 mM HEPES (Gibco), 2g L^{-1} sodium bicarbonate (Sigma Aldrich), 2g L^{-1} glucose (Sigma Aldrich), 100 mg L^{-1} calcium nitrate (Sigma Aldrich), 400 mg L^{-1} potassium chloride (Sigma Aldrich), 6 g L^{-1} sodium chloride (Sigma Aldrich), 800 mg L^{-1} sodium phosphate dibasic (Sigma Aldrich), 1 mg L^{-1} Glutathion (Sigma Aldrich), 50 U m^{-1} penicillin and 50 µg mL^{-1} streptomycin and 10% HI dialyzed FCS (dFCS, Gibco). For functional readouts, the medium was either supplemented, as indicated, with 1.2 mM $MgCl_2$ or 0.05 mM $MnCl_2$ or left untreated (= 0 mM Mg^{2+}). Cells of every condition were washed initially twice in magnesium-free medium prior to any functional read out. Low background Mg^{2+} values in *self-made* medium was verified by ICP-MS (data not shown).

Cell Lines

Jurkat T cells (Clone E61, TIB-152) and HEK-293T were purchased from ATCC. T2 cells and EL4 were kindly provided by A. Zippelius (University of Basel). MC38-OVA were provided by P. Romero (University of Lausanne). PC3-PIP cell lines were provided by A. Rosato (University of Padua, Padova).

Mice

C57BL/6, MHC class I-restricted OVA-specific T cell receptor (OT-I) transgenic and B6.129S7-Itgaltm1Bll/J (LFA-1 KO) mice were originally purchased from Jackson Laboratories (USA) and thereafter bred and housed at specific pathogen free (SPF) conditions at the University of Basel. CAR

T cell experiments were conducted with NSG mice which were bred and housed in a specific and opportunistic pathogen-free animal facility in the Oncology Department of the University of Lausanne. Age and sex matched C57BL/6 mice were purchased from Charles River (Italy) for intratumoral Mg^{2+}-application experiments. Mice were maintained at SPF conditions and acclimatized for 1 week prior to experiments at the animal facility of the University of Geneva. All experiments were conducted in accordance to the Swiss Federal Veterinary Office guidelines and were approved by the Cantonal Veterinary Office (Canton of Basel-Stadt, Vaud and Geneva). All cages provided free access to food and water. During experimentation, all animals were monitored at least every other day for signs of distress and, if required, body weight was measured three times a week. Mice were sacrificed at the endpoint by carbon dioxide overdose.

Chemicals

LFA-1 inhibitor studies were performed using BIRT377 at 50µM (Tocris). TCR independent activation of T cells were conducted with PMA (50 ng mL^{-1}; Sigma Aldrich) and ionomycin (1 µg mL^{-1}; Sigma Aldrich). All chemicals were aliquoted in DMSO and stored at -20°C until used.

Flow cytometry

Either a BD Fortessa LSR II (BD Bioscience) or Cytoflex S (Beckmann) flow cytometer were used for flow cytometry.

For analysis of surface markers, T cells were harvested at indicated time points after activation *in vitro*, washed once in cold PBS and, if required, stained with Fixable Viability Dyes for 15 min at 4°C. Surface markers were stained with appropriate antibodies for 20 min at 4°C.

For stainings of cell suspension from murine organs, cells were additionally pre-incubated with anti-mouse Fc block 10 µg mL^{-1} (anti-CD16/CD32, BioXCell).

For intracellular TNF staining, cells were activated for 4 hours as indicated. During the final 2 hours of activation, cells were treated either with brefeldin A solution (BioLegend) to block cytokine secretion. Cells were then washed and fixed for 20 min at RT (fixation/permeabilization solution, BD Biosciences) and washed with permeabilization buffer (BD Biosciences) prior to staining for 45 min and further washing before acquisition.

For analysis of protein phosphorylation, T cells were stimulated as indicated and stained as previously described [59]. Briefly, cells were fixed by adding 8% Paraformaldehyde (PFA) (Thermo Fisher) directly into the culture medium to obtain a final concentration of 4% PFA. Cells were incubated for 15 min at RT, washed with FACS buffer, followed by permeabilization with ice cold methanol at 4°C for 5 min. After washing with FACS buffer, cells were stained at room temperature for 30 min, washed and acquired.

For evaluation of activation-induced LFA-1 extension, T cells were activated for 45 min and anti-human CD11a/CD18 (clone m24) was directly added in medium and incubated on ice for 20 min. Cells were then washed twice in FACS Buffer and fixed in 2% PFA, incubated at room temperature for 20 min and washed with FACS Buffer before acquisition.

For 2-NBDG uptake assays, previously activated T cells were co-incubated for last 45 min of experiment directly with a final concentration of 20 µM 2-NBDG (Biolegend). Cells were washed twice in FACS buffer before acquisition.

For staining the following antibodies were used:

MC38-OVA tumor model: CD3 (BV480, BD Bioscience), $CD8^+$ (BV421, BD Bioscience) CD44 (SB645, eBioscience), CD45 (BUV395, BD Bioscience), CD107a (APC, Life technologies), Ki67 (FITC, eBioscience), Tetramer anti-H-2 Kb OVA (PE, Immudex), IFNγ (BUV737, BD Bioscience), Viability dye (Near IR, Life technologies).

Murine peritonitis model: $CD8^+$ (FITC, Biolegend), CD11b (PE-Cy5, Biolegend), CD11c (PE-Cy5, Biolegend), CD69 (APC, Biolegend), CD107a (PE/Cy7, Biolegend), B220 (PE-Cy5, Biolegend), F4/80 (PE-Cy5, Biolegend), Tetramer H-2 Kb OVA (PE, Tetramers core facility, University of Lausanne), Viability Dye (Zombie Red, BioLegend,)

Murine in vitro activation: CD11a (FITC and BV421, Biolegend), LFA-1 (BV421, Biolegend), $CD8^+$ (FITC, Biolegend), CD69, (APC, Biolegend), CD107a (PE-Cy7, Biolegend), phospho-ERK1/2 (AF647, Biolegend), Viability Dye (Aqua Zombie, Biolegend).

Human in vitro activation: CD11a (FITC, Biolegend), CD18 (PE, Biolegend), CD25 (APC, BD), CD45RA (Pacific Blue, Beckmann), CD62L (APC, Immuno Tools), CD69 (PerCP, Biolegend), CD71 (PE, Biolegend), CD107a (AF647 BD and PE-Cy7, both Biolegend), CD98 (FITC, BD Bioscience and Biolegend), m24 epitope LFA-1 (PE, Biolegend), phospho-c-Jun (unlabeled, Cell Signaling Technology), phospho-ERK1/2 (AF647, Biolegend), goat anti-rabbit IgG (AF488, Thermo Fisher), TCR Vbeta13.1 (FITC and PE-Cy7, Biolegend), TNF (PE, Biolegend), Viability Dye (Aqua Zombie, Biolegend; Zombie Green, BioLegend).

Murine MC38-OVA tumor model

Unless stated otherwise, 6 to 12 weeks old female mice were used for experiments. In assays with pre-immunized mice, mice were immunized 19 days before tumor implantation by subcutaneous injection of 15 µg of $OVA_{257–264}$ peptide (Invivogen) and 50 µg of CpG-B ODN 1826 (Eurogentec), resuspended in 100 uL of PBS. For tumor implantation, mice were inoculated subcutaneously onto the flanks with 0.5×10^6 MC38-OVA cells, resuspended in 100 uL of PBS. In bilateral tumor experiments, mice received 50 uL intra-tumoral injections of either 3 mM NaCl or 3 mM $MgCl_2$ (both diluted in ddH_2O) 7 days after tumor implantation. Injections of NaCl solution was applied in left flank tumor, whereas $MgCl_2$ solution was injected in contralateral tumor. This regimen was repeated every third

day for a total of 8 cycles. Tumor size was quantified using a caliper and tumor volume was calculated using a rational ellipse formula ($\alpha^2 \times \beta \times \pi/6$, α being the shorter axis and β the longer axis). Excised tumors were weighed post-mortem. In all survival experiments, mice were withdrawn from the study after any tumor dimension had reached a length greater than 15 mm.

***In vivo* PD-1 blockade**

For PD-1 blockade experiments, mice were immunized with OVA, as described above, and inoculated with 0.5×10^6 MC38-OVA cells unilaterally on the flank. From day 5, intratumoral injections of either 3 mM NaCl or 3 mM $MgCl_2$ were initiated, and repeated every third day for 8 cycles. Mice were additionally injected i.p. with isotype control (IgG2a) or anti-PD-1 Ab on day 9, 12, and 15 post-tumor implantations, at a dose of 200 µg per mouse diluted in 100 µL of pH-matched PBS (according to manufacturer's recommendations). The antibodies used were: anti-PD-1 IgG2a Ab (clone RMP1-14) or IgG2a isotype control Ab (clone 2A3, bot purchased from BioXCell).

Flow cytometric analysis of tumor infiltrating immune cells

For analysis of tumor infiltrating immune cells; tumor inoculation, intratumoral ion injections and antibody treatment were performed as described above. Additionally, 7 days post-tumor inoculation, all mice were boosted with peritumoral s.c. injection of 100 ug endotoxin-free OVA protein (Hyglos) and 50 ug CpGB-ODN 1826 resuspended in 100 uL of PBS. At day 20 post-tumor inoculation, mice were sacrificed and tumors and TdLN were excised. TdLNs were processed through a 70 µm nylon mesh. Tumors were minced, processed through a 70 µm nylon mesh, and digested with Collagenase D and DNAse I (Roche) in HBSS (Gibco) for 40 min at 37 °C. Single cell suspension were *in vitro* reactivated with 50 ng mL^{-1} PMA and 1 ug mL^{-1} Ionomycine for 4.5 hours in presence of 1 ug mL^{-1} Golgi-plug and 1 ug mL^{-1} Golgi-stop (Becton Dickinson) in full RPMI-1640. Cells were then further processed as described above and acquired by FACS.

Magnesium restricted diet

Magnesium restricted diet and matching control diet, based on the purified ingredient rodent diet *AIN-76A*, were purchased at Research Diets Inc. (USA).

Sample collection of tissue interstitial fluid

Healthy C57BL/6 mice (male and female, 6-10 weeks, groups were sex and age adjusted) were kept on magnesium restricted diet or corresponding control diet for 2 weeks. At day 14, liver, spleen and peripheral lymph nodes, muscle (musculus quadriceps femoris) and subcutaneous fat (flank) were aseptically removed. Organs were weighed, 50-300 ul PBS added (adjusted according to weight), and gently centrifuged at 300 x g for 8 min. Organ supernatants were recovered and stored at -80°C. Peritoneal lavage was conducted as described above. Tissue interstitial fluid of tumors from *in vivo* CAR T cell experiments were collected from UTD and saline control mice reaching ethically acceptable

end point. Tumors were aseptically excised, weighed and supernatant was recovered as described above.

Magnesium measurements with ICP-MS

Samples of varying volumes (serum 5 µl; Muscle 10 µl; liver, lymph node, peritoneal fluid, subcutaneous fat and tumor 25 µl; spleen 50 µl) were added to 200 µl 67-69% HNO_3 (VWR Chemicals; NORMATOM® grade; LOT 1119100) and incubated at 95°C for 2 hours. Digestates were filled up to 5 mL volume using ultra-pure H_2O (<18mΩ; Merckmillipore, 115333) and stored at 4°C. Samples were analyzed using triple quadrupole inductively coupled plasma mass spectrometry (qqq-ICP-MS) on an 8800 system (Agilent, Basel, Switzerland), using general-purpose operational settings. The system was operated in single quad mode using helium as collision gas and quantification done on $^{24}Mg^{+}$. To account for matrix effects, ^{103}Rh was used as the internal standard. Organ Mg^{2+} levels were normalized to tissue weight.

Blood count mice

Blood samples (70uL) were harvested in EDTA-coated tubes and diluted with 210uL NaCl 0.9%. Samples were run on the ADVIA 2120i hematology analyzer (Siemens) and analyzed by the multi-species program.

***In vivo* killing assay**

C57BL/6 mice (male and female, 6-10 weeks, groups were sex and age adjusted) were immunized against OVA at day -19. In a first experiment, mice were immunized s.c. with 100 µg OVA protein (Invivogen) and 50 µg of CpG-B (Invivogen). In a second experiment, mice were immunized i.v. with 5×10^3 CFU LmOVA. On day 0, mice were put on magnesium-restricted or control diet for two weeks. On day 14, target splenocytes were harvested from naïve, syngeneic mice and either loaded with $OVA_{257–264}$ peptide (Eurogentec) or left untreated. Unloaded control splenocytes were labeled brightly with 2.50 µM CTV (CTV^{bright}) and $OVA_{257-264}$-loaded splenocytes dimly with 0.25 µM CTV (CTV^{dim}). Cells were then counted, mixed at 1:1 ratio in PBS, and $2\text{-}4\times10^6$ total target splenocytes were injected i.v. into pre-immunized and naive control mice. Additionally, 200 µl of 3 mM $MgCl_2$ and 200 µl of 3 mM NaCl were administered i.p., respectively. After 12 hours, spleens were harvested and splenocyte suspensions were analyzed by flow-cytometry. Percentages of specific *in vivo* killing were calculated as [1-(% CTV^{dim} naive / % CTV^{bright} naive) / (% CTV^{dim} immunized / % CTV^{bright} immunized)]×100.

Listeria peritonitis model

C57BL/6 mice (male and female, 6-10 weeks, groups were sex and age adjusted) were immunized i.p. with 5×10^4 CFU Listeria monocytogenes expressing the OVA-peptide (LmOVA). After 19 days, mice were put on Mg^{2+}-restricted or matching control diet for 2 weeks. Mice were then re-infected i.p. with 5×10^5 CFU LmOVA. Bacterial inoculum was either spiked with 3 mM $MgCl_2$ or 3 mM NaCl diluted in

200 µl ddH_2O. Mice were sacrificed 12 hours post infection and peritoneal fluid was harvested. Peritoneal fluid was harvested upon injection if 10 mL sterile PBS into peritoneal cavity; peritoneum was gently massaged and then aseptically opened by incision and lavage was collected. Peritoneal fluid was then plated on BHI agar-plates and colonies counted upon 24 hours of incubation. Remaining peritoneal fluid were centrifuged at 300 x g for 10 min and supernatant recovered. Peritoneal fluid and sera were frozen at -80°C prior to further analysis. For flow cytometric analysis of memory $CD8^+$ T cell compartment, mice were scarified 20 hours post infection, and peritoneal fluid was harvested. MACS beads and LS columns (both Milteny Biotec) were used to enrich cell suspension for $CD8^+$ T cells. Cells were stained as described above and analyzed by FACS.

Cytometric bead array (CBA)

Cytokine concentrations in cell culture supernatants, peritoneal fluids and were determined using the LegendPlex cytrometric bead Array Th1-Pannel (human and mouse, both from Biolegend) according to manufacturer's instructions.

Perforin quantification

Perforin concentrations in peritoneal fluids were determined using ProQuantumMouse Granzyme B Immunoassay Kit (Inivtrogen) according to manufacturer's instructions.

Human naïve and memory T cell isolation

Blood samples were obtained from healthy male and female donors (18-65 years old) as buffy coats after written informed consent (Blood donor center, University Hospital Basel). Peripheral blood mononuclear cells (PBMCs) were isolated by standard density-gradient centrifugation protocols (Lymphoprep; Fresenis Kabi). MACS beads and LS columns (both Milteny Biotec) were used to sort $CD8^+$ positive T cells. The positively selected $CD8^+$ T cells were incubated with APC anti-CD62L mAb (ImmunoTools) and Pacific Blue anti-CD45RA (Beckman Coulter). Naïve and EM $CD8^+$ T cells were identified as $CD62L^+$ $CD45RA^+$ and $CD62L^-$ $CD45RA^-$ populations, respectively. Cell sorting was performed using a BD FACSAria III or BD influx cell sorter (BD Bioscience). Cells were rested for 24 h at 37°C prior to further experiments.

Metabolic assays

A Seahorse XF-96e extracellular flux analyzer (Seahorse Bioscience, Agilent) was used to determine the metabolic profile of cells. T cells were plated (2×10^5 cells/well) onto Celltak (Corning, USA) coated cell plates. Experiments were carried out in unbuffered, serum- and Mg^{2+}-free *self-made* medium. Medium was reconstituted with 1.2 mM $MgCl_2$ or 0.05 $MnCl_2$ as indicated in individual experiments. Reconstitution of cations was either present from beginning of experiment or applied onto plated cells via the instrument's multi-injection port. All following concentration represent final well concentrations of indicated substance. Human T cells were activated by injection anti-CD3 Ab (1 µg

mL^{-1}), or anti-CD3 Ab (1 µg mL^{-1}) and anti-CD28 Ab (10 µg mL^{-1}), or PMA (50 ng mL^{-1}; Sigma Aldrich) and ionomycin (1 µg mL^{-1}; Sigma Aldrich). In certain experiments (as indicated) anti-CD3/CD28 antibodies were cross-linked with additional injection of secondary goat anti-mouse Ab (5 µg mL^{-1}, Thermo Fisher). Murine T cells were activated by injection anti-CD3 Ab (5 µg mL^{-1}) and anti-CD28 Ab (2.5 µg mL^{-1}). Glycolytic switch was quantified by subtracting maximal ECAR from baseline ECAR-measurements. Mitochondrial perturbation experiments were carried out by sequential addition of oligomycin (1 µM, Sigma Aldrich), FCCP (2 µM, Carbonyl cyanide 4-(trifluoromethoxy) phenylhydrazone, Sigma Aldrich), and rotenone (1 µM, Sigma Aldrich). Glycolysis stress test was performed in medium as described above but devoid of glucose. Sequential injections of glucose (10 mM, Sigma Aldrich), oligomycin (1 µM) and 2-deoxy-glucose (50 mM, Sigma Aldrich). Oxygen consumption rates (OCR, pmol/min) and extracellular acidification rates (ECAR, mpH/min) were monitored in real time after injection of each compound.

Generation of human T cell blasts (PHA-blasts)

PBMCs were obtained as described above and activated with 10 µg mL^{-1} Phytohaemagglutinin (PHA, Thermo Fisher) and 300 U mL^{-1} human recombinant IL-2 (Proleukin, Novartis). PHA-blasts were expanded by adding fresh IL-2 every 3-4 days.

***In vitro* activation primary human T cells and PHA-blasts**

Unless stated otherwise, human EM $CD8^+$ T cells and PHA-blasts were activated in presence of plate-bound anti-CD3 Ab (HIT3a, Biolegend) at 1 µg mL^{-1} and soluble anti-CD28 Ab (CD28.2, Biolegend) at 5 µg mL^{-1}. Naïve $CD8^+$ T cells were activated with in-house generated anti-CD3/anti-CD28 coated microbeads. Polybead microspheres (4.5 mm, Polyscience Eppenheim) were incubated with 1 µg anti-CD3 Ab and 10 µg anti-CD28 Ab. T cells were plated at 2×10^5 cells per well in flat bottom 96 well plates (Greiner Bio One) in self-made medium supplemented with 10% dFCS and indicated supplementation of cations or LFA-1 inhibitor. Primary human T cells were activated for 24 h and PHA-blasts for 4 hours.

Under-agarose migration assay

Glass bottom µ-slides (ibidi; Cat.#: 80827) were coated with 10 µg mL^{-1} human plasma fibronectin (Merck; Cat.#: FC010) in PBS for 1 h at 37°C and then washed with PBS. Prior to gel casting, 10 mL 2x HBSS ± 2.4mM $MgCl_2$ and 20mL self-made medium ± $MgCl_2$ was warmed to 68°C in a water bath. Then 0.48 g of ultra-pure agarose (Invitrogen; Cat.#: 16500-100) was dissolved in 10 mL ddH_20, heated to boiling and vortexed until all particles were dissolved. The agarose was mixed with the prewarmed HBSS/medium to a 1.2% agarose solution and then casted into the coated dish at 300 µL per well. After cooling down at RT for 30 min, the gels were incubated for 1 h at 37°C and 5% CO_2. For the cell loading the cells were resuspended at 1×10^7 mL^{-1} and 5×10^5 cells were injected under the gel with a gel-loading pipette and imaging commenced right after. The cells were imaged with a 10x CFI Plan Apo

Lambda (NA 0.45) objective on a Nikon TI-E in the BF channel with a frequency of 2 fpm. The data was manually tracked with the "Manual Tracking" plug in Fiji. A custom-written code in R was used for data processing and plotting.

Venn Diagram

Venn diagram visualizes the following gene lists: metal ion binding (GO:0046872), leukocyte cell-cell adhesion (GO:0007159), leukocyte migration (GO:0050900), immunological synapse (GO:0001772) and differentially expressed protein between naïve and memory $CD8^+$ T cells (memory>naïve) [32]. Venn diagram was made with InteractiVenn online tool [60].

CRISPR-Cas9 editing of murine OT-1 cells and human Jurkat T cells

crRNAs were selected from predesigned CRISPR-Cas9 guide RNAs Tool from IDT. Product ID and sequences are listed in **Supplemental Table 1**. crRNA (IDT) or negative control crRNA #1 (IDT) and trRNA (IDT) were mixed at a 1:1 ratio to a final concentration of 50 µM in nuclease-free duplex buffer (IDT), annealed at 95°C for 5 min and added to 40 µM Cas9 (QB3 MacroLab, UC Berkeley) followed by incubation at room temperature for at least 10 min. Murine OT-1 cells were nucleofected with the Mouse T Cell Nucleofector Kit (Lonza) according to manufacturer's instructions using 2b Nucleofector. Briefly, single cell suspensions were made from lymph nodes and spleens harvested from OT-I mice (male and female, 6-10 weeks, equal distribution of sex and age). 2×10^6 OT-I lymphocytes were resuspended in 100 µl of Nucleofector Solution and combined with 20 µM RNP. An appropriate nucleofector program was applied. Cells rested in Mouse T Cell Nucleofector Medium (Lonza) for 24 h and were then activated with $OVA_{257–264}$ peptide pulsed (10^{-9} M) C57/Bl6 splenocytes for 3 days in presence 100 U mL^{-1} of IL-2 (Proleukin). Cells were washed and seeded in fresh medium at 10^6 mL^{-1} in round bottom 96 well-plates with 500 U mL^{-1} IL-2. Knock-out efficiency was validated by flow cytometry and purified by cell sorting. Jurkat T cells were nucleofected as described above using the AMAXA cell line V nucleofection kit (Lonza). Knock-out efficiency was validated by flow cytometry and purified by cell sorting. Jurkat T cells were initially expanded for 1 week and then stored in liquid nitrogen until further use.

Calcium Flux Assay

Jurkat T cells were loaded with Fluo4 (Invitrogen) at a final concentration of 2 µM in Mg^{2+}-free self-made medium for 30 min at 37°C. Cells were washed twice and plated at 2×10^5 per well in a black flat bottom 96 well-plate (Greiner BIO-one) which had been precoated with collagen (Thermo Fisher) to enhance cell attachment. An additional incubation for 15 min at 37°C allowed cells to adhere and Fluo4 probe to de-esterified completely. Jurkat T cells stimulated with 10 µg mL^{-1} anti-CD3. Fluorescence intensity over time was measure with a Tecan Spark M10 plate reader. Samples were

run in technical duplicates and the mean of fluorescent signal intensity was normalized to unstimulated baseline values.

Murine CTLs: differentiation and cultivation

Single cell suspensions were made from lymph nodes and spleens harvested from C57Bl/6 and LFA-1 KO mice (male and female, 6-10 weeks, equal distribution of sex and age). Naïve $CD8^+$ T cells were isolated using a magnetic bead-based negative selection kit following the manufacturer's recommendations (easySEP, Stem Cell technology). Naïve T cells (2×10^5 per well) were plated in presence of 5 µg anti-CD3 Ab (plate-bound) and 1µg anti-CD28 Ab (soluble; both from Biolegend) for 2 days in presence 100 U mL^{-1} of IL-2 (Proleukin). Cells were washed and seeded in fresh medium at 10^6 mL^{-1} in round bottom 96 well-plates with 500 U mL^{-1} IL-2. A cell density of 0.5–2 × 10^6 cells mL^{-1} was maintained for expansion and IL-2 was replaced on a daily basis. Functional read outs were carried out 7-19 days after initial activation and in the absence of IL-2.

Murine CTLs: *In vitro* activation and cytotoxicity assay

CTLs of WT or LFA-1 KO C57/Bl6 were activated for with plate-bound anti-CD3 Ab (145-2C11, Biolegend) at 0.05 µg mL^{-1} and soluble anti-CD28 Ab (37.51, Biolegend) at 1 µg mL^{-1} at 2×10^5 cells per well in a flat bottom 96 well plate. For stainings of surface activation markers, CTLs were activated for 8 h and for evaluation of 2-NBDG uptake, cells were activated for 6 h. For analysis of ERK1/2 phosphorylation, CTLs were stimulated with 5 µg mL^{-1} anti-CD3 Ab and 1 µg mL^{-1} anti-CD28 for 20 min prior to fixation and permeabilization.

For cytotoxicity assays with WT or LFA-1 KO C57/Bl6 derived CTLs, cytotoxicity was evaluated with NucView 488 fluorogenic caspase-3 substrate (Biotium). Prior to co-incubation, CTLs were labeled with CellTrace Violet (CTV, Invitrogen) and EL4 target cells with carboxyfluorescein diacetate succinimydyl ester (CFSE, Invitrogen). Both cell population were then co-incubated at a CTL-target cell ratio of 3:1 in presence of 10 µg mL^{-1} PHA for 4 hours in a flat bottom 96 well plate. Caspase-3 substrate was added for final 45 min of incubation at final concentration of 1 µM. Cells were harvested, washed in FACS Buffer and fixed with PFA 2% for 15 min at RT prior to analysis by FACS.

For cytotoxicity assays with OT-I derived CTLs, luciferase-expressing EL4 target cells were pulsed with $OVA_{257–264}$ peptide (SIINFEKL, Eurogentec) or the altered peptide ligands R7 (SIIQFERL, Eurogentec), H7 (SIIQFEHL, Eurogentec) or G4 (SIIGFEKL, Eurogentec) at 1 µM for 30 min. EL4 target cells were washed 3 times prior to co-incubation at a CTL-target cell ratio of 3:1 for 4h. Cytotoxicity was quantified after adding luciferin at 0.15 mg mL^{-1} (PerkinElmer) to medium and measuring luminescent signal intensity by plate reader (Synergy H1, BioTek).

Imaging of immune synapse with confocal microscopy

Pictures from immunofluorescence imaging were recorded on a Nikon Ti with a Yokogawa CSU-W2 spinning disk module on a Photometrics 95B (22mm back-illuminated sCMOS) camera. A Nikon CFI Apo Lambda 60x objective or Nikon CFI Apo TIRF NA 1.49 100x objective was used with 1.515 oil mounted samples. Diode-pumped solid-state lasers at 405, 488, 561, and 647nm were used together with filters for DAPI (ET460/50nm), AF488 (ET525/50nm), AF555 (ET630/75nm) and AF647 (ET700/75nm) with a Quad BS Dichroic mirror. If required, raw nd2 format image stacks were deconvoluted using Huygens using a theoretical point spread function classical maximum likelihood estimation using 100 iterations and a quality stop criterion of 0.05.

Immunofluorescent staining of immune synapse components in Jurkat T cells, PHA blasts and murine CTLs

Cells were activated on species-appropriate anti-CD3-coated (1 µg mL^{-1} for human cells, 0.05 µg mL^{-1} for murine cells) glass-coverslips (Thermo Fisher) for 2 min for phosphor-tyrosine analysis and 5 min for organelle translocation experiment. Cell conjugates were fixed for 20 min at RT in 4% methanol-free PFA (Sigma Aldrich), permeabilized with 0.1% Triton-X100 (Sigma Aldrich) in PBS for 5 min and quenched with 50mM Glycine (Sigma Aldrich) in PBS for 20 min. Fixation was followed by blocking in 1% bovine serum albumin (Sigma Aldrich) in PBS (blocking buffer) for 45 min at 4°C. Primary antibodies were then incubated in the same blocking buffer for 1 hour at RT or overnight at 4°C. Samples were then washed four times with blocking buffer, followed by incubation with secondary antibodies in blocking buffer at room temperature for 1 hour. Slides were then mounted with Prolong Diamond Antifade Mountant (Thermo Fisher) and analyzed after 24 h of curing time at RT.

The following reagents and antibodies were used for staining: phospho-tyrosine *P-Tyr-1000* (multiple monoclonal antibodies, unlabeled, Cell Signaling Technology), Granzyme B (clone QA16A02, FITC, Biolegend), aTOM20 (clone D8T4N, unlabeled, Cell Signaling Technology), secondary goat anti-mouse (AF488, Thermo Fisher), secondary goat anti-rabbit (AF647, Thermo Fisher), Phalloidin-iFluor (AF555, Abcam) and DAPI (Sigma Aldrich).

Image analysis of organelle translocation experiment with murine CTLs

For Granzyme B and mitochondria detection, series of confocal *Z*-stacks were first processed by Fiji software and maximum intensity z-projections were made out of 11 consecutive slices (0.1 µm) closest to anti-CD3-coated coverslip bottom (region of *pseudo* immune-synapse) using *Z project*-tool. Using Imaris software (Bitplane), Granzyme B staining was quantified with *spot*-tool: source channel 1 = 488, 0.7 µm estimated diameter and spot classification with quality threshold > 113. Mitochondria area was quantified with *surface*-tool: source channel 2 = 647, diameter cut-off of 1.38 µm with a surface detail of 0.2 µm, manual threshold adjustment and surface classification > 10 voxels. Cell number was quantified by number of nuclei using *spot*-tool: source channel 4 = DAPI, 7 µm estimated diameter

and spot classification with quality threshold > 39. Sum of mitochondria area and number of Granzyme B spots were normalized to cell number (defined by number of nuclei) per field of view.

Image analysis and quantitation of phosphor-tyrosine signal intensity

For measurement of pan-phospho tyrosine signal intensity, FiJi software was used. Series of confocal Z-stacks were displayed as maximum intensity z-projections using *Z project*- tool. Individual cells were selected manually with *freehand selection*-tool according to cell boundaries indicated by phalloidin staining and fluorescent intensity was measured accordingly with *measure*-tool.

Immunoblot analysis

Memory T cells and PHA-blasts were lysed in RIPA buffer (Thermo Fisher) containing protease- and phosphatase-inhibitors (Roche, #05 892 970 001 and #04 906 837 001), and protein concentrations determined with a BCA protein assay kit (Thermo Fisher). Whole-cell lysates were denatured with 4x Laemmli buffer and separated by 4-20% SDS-PAGE and transferred to nitrocellulose or PVDF membranes (Biorad). Membranes were probed with the following primary antibodies: P-p44/42 MAPK (Erk1/2, Thr202/Tyr204, #D13.14.4E, Cell Signaling Technology), P-c-Jun (S73, #D47G9, Cell Signaling Technology), p44/42 MAPK (Erk1/2, #137F5, Cell Signaling Technology), c-Jun (#60A8, Cell Signaling Technology) and Actin (#8H10D10, Cell Signaling Technology). Blots were then stained with HRP-conjugated anti-rabbit or anti-mouse (both from Jackson ImmunoResearch Laboratories) secondary antibodies. SuperSignal West Pico PLUS Chemiluminescent Substrate (Thermo Fisher) according to the manufacturer's instructions and ChemiDoc Imaging System (Biorad) were used for detection and FiJi software for quantification.

NY-ESO Peptides

NY-ESO-9c peptide (SLLMWITQC) was purchased in >95% purity from EZ Biolabs. Lyophilized peptides were resuspended at 10mM in sterile dimethyl sulfoxide (DMSO) and stored at -20°C until further use.

T Cell Receptor Construct for REP T cells

The lentiviral construct encoding for the codon-optimized WT LAU155 NY-ESO-1 T cell receptor α and β chains under an hPGK promotor separated by an IRES domain was kindly provided by M. Hebeisen and N. Rufer at the University of Lausanne [61,62]. This TCR has a K_D = 21.4 μM for its endogenous NY-ESO-1 SLLMWITQC peptide.

Generation of lentivirus for REP T cells

To generate lentivirus, 2.5×10^6 low passage HEK293T cells were cultured in DMEM medium (Thermo Fisher) and seeded into a 15 cm tissue-culture treated dish. After 3 days, 2nd generation LTR-containing donor plasmid, packaging plasmid pCMV-delta8.9 and the envelope plasmid VSV-G were mixed at a 4:2:1 ratio in non-supplemented Opti-MEM (Thermo Fisher) and sterile filtered. This solution was then mixed with polyethyleneimine 25 kDa (Polysciences Inc.), also diluted in Opti-MEM at a DNA:PEI ratio

of 1:3. 28 μg of DNA was transfected per 15 cm dish. After 2 days, supernatants were collected from cells (exchange medium) and filtered through a 0.45 μm PES filter. Supernatants were stored for 1 day at 4°C until the second batch of supernatant was collected 24 h later. The supernatant containing lentiviral particles was concentrated by ultra-centrifugation at 40,000 x g for 2 hours at 4°C, resuspended in 0.1% BSA in PBS, and frozen to -80°C until further use.

Transduction of human T Cells for REP T cell production

To generate NY-ESO-1 TCR specific T cells, human healthy donor PBMC were thawed and washed in PBS. $CD8^+$ T cells were then isolated using the $CD8^+$ microbeads (Miltenyi) according to the manufacturer's instructions on an AutoMACS (Myltenyi). Isolated cells were washed and resuspended in medium supplemented with 150 U mL^{-1} IL-2 and plated at 1.5 mio mL^{-1}. $CD8^+$ T cells were then activated at a 1:1 ratio with activation beads from T cell activation and expansion kit (Miltenyi) according to manufacturer's instructions. 24 hours later, NY-ESO-1 TCR lentiviral particles, produced as described above, were added at a multiplicity of infection (MOI) of 2. Cells were then expanded every 2 days with fresh medium and replenishing 50 UmL^{-1} IL-2 for 5 days. NY-ESO-1 TCR positive T cells were sorted using a FACSAria III or FACS SorpAria (BD) and re-stimulated with NY-ESO-9c peptide. A cell density of 0.5–2×10^6 cells mL^{-1} was maintained for expansion and 3,000 U mL^{-1} IL-2 replaced ever third day. After 1 week of expansion, cells were either stored in liquid nitrogen or further expanded and subsequently used for functional read outs as described below.

REP T cells: activation *in vitro* and cytotoxicity assays

REP T cells were incubated with T2 target cells in flat bottom 96 well-plate at a 1:1 ratio (4-6×10^4 each). In order to distinguish the different cell populations, REP T cells were labeled with CTV and T2 target cells with CFSE, Invitrogen. Prior to co-incubation, T2 target cells were pulsed with NY-ESO-9c peptide at 10^{-8} M for 30 min in magnesium-free medium before being washed and re-suspended with REP T cells in magnesium-free medium supplemented with 10% dFCS at indicated cation or LFA-1 inhibitor concentration. For all co-incubation experiments, cells were allowed to sediment without centrifugation.

For analysis of protein phosphorylation, co-incubation was terminated after 25 min as described above. In these experiments, Mn^{2+} concentration was 0.5 mM instead of 0.05 mM as in all other experiments.

For degranulation assays, an anti-CD107a-AF647 Ab was added directly into culture medium throughout the entire co-incubation. After 4 hours, cells were harvested, washed in cold FACS Buffer and gently fixed with PFA 2% for 15 min at room temperature.

Cytotoxicity was examined with NucView 488 fluorogenic caspase-3 substrate (Biotium). Fluorogenic caspase substrate was added to wells at the beginning of co-incubation at final concentration of 1 μM.

After 45 min, cells were washed in FACS Buffer and gently fixed with PFA 2% for 15 min at room temperature.

Immunofluorescent staining of immune synapse components of REP T cell/T2 cell conjugates

REP T cells and T2 target cells were individually labeled with CTV or CFSE. T2 cells were loaded with 10^{-7} M NY-ESO-9c peptide for 30 min. T2 and REP T cells were washed three times in serum- and Mg^{2+}-free medium, mixed 1:1 and resuspended to a final concentration of 2.5×10^{6} cells mL^{-1}. Cell suspension was incubated 5 min at RT, before aliquoting in 50 µl onto glass multiwell slides (Thermo Fisher) and incubating for indicated time. Cell conjugates were fixed for 20 min at RT in 4% methanol-free PFA (Sigma Aldrich), permeabilized with 0.1% Triton-X100 (Sigma Aldrich) in PBS for 5 min and quenched with 50mM Glycine (Sigma Aldrich) in PBS for 20 min. Fixation was followed by blocking in 1% bovine serum albumin (Sigma Aldrich) in PBS (blocking buffer) for 45 min at 4°C. Primary antibodies were then incubated in the same blocking buffer for 1 hour at RT or overnight at 4°C. Samples were then washed four times with blocking buffer, followed by incubation with secondary antibodies in blocking buffer at room temperature for 1 hour. Slides were then mounted with Prolong Diamond Antifade Mountant (Thermo Fisher) and analyzed after 24 h of curing. Of note, for visualization of extended LFA-1, m24 antibody was added directly in multi-well slides during co-incubation and cells were fixed after 10 min.

The following reagents and antibodies were used for staining: CD11a/CD18 (clone m24, Biolegend), gamma Tubulin (clone EPR16793, Abcam), perforin (clone δG9, BD Bioscience), phospho-tyrosine P-Tyr-1000 (#8954S, Cell Signaling Technology), secondary goat anti-mouse (AF568, Thermo Fisher), secondary goat anti-rabbit (AF647, Thermo Fisher) and DAPI (Sigma Aldrich)

Image analysis and quantitation of REP T cell-T2 target cell conjugates

For analysis of extended LFA-1 and pan phospho-tyrosine intensity in REP T cells, confocal *Z*-stacks were acquired and analyzed using Imaris software (Bitplane). REP T cell volumes were identified using the *surface*-tool: source channel 4 (DAPI = CTV), 5 µm diameter cut-off with 0.369 µm surface detail and > 1689 voxels. Fluorescent signal of source channel 3 (AF555 = LFA-1 m24 staining) outside of REP T cell-surface was masked and extended LFA-1 was quantified with *surface*-tool: source channel 5 (masked AF555), 1.39 µm diameter cut-off with 0.369 µm surface detail and > 154 voxels. Number of LFA-1 m24-objects were normalized to REP T cell number per field of view. Pan phospho-tyrosine intensity was determined by plotting *median intensity* of source channel 2 (AF647) per REP T cell volume identified as described above.

For analysis of perforin and centrosome polarization, position of REP T and T2 target cells in confocal *Z*-stacks were characterized with *spot*-tool: Source channel 1 (AF488 = CFSE) with the following parameters 10 µm estimated diameter and spot classification with quality threshold > 27.4 was used

to identify T2 target cells and source channel 4 (DAPI = CTV) with 8 µm estimated diameter and spot classification with quality threshold > 37.8, for REP T cells respectively. For detection of centrosome and perforin granules in REP T cells *surface*-tool was applied on source channel 4 (DAPI = CTV), 5 µm diameter cut-off of with 0.369 µm surface detail and > 2014 voxel cut-off. Fluorescent signal of source channel 1 (AF488 = perforin) and source channel 2 (AF647 = centrosome) outside of defined REP T cell surface was masked and positions of respective objects were identified with *spot*-tool: 0.8 µm estimated diameter and spot classification with quality threshold > 1365 for perforin and 1.84 µm estimated diameter and spot classification with quality threshold > 637 for centrosome. X, Y, Z values of each individual spot (cells, perforin granule and centrosome) were subjected to further analysis using script in R. For each spot we identified its parent T cell and for each T cell its nearest tumor cell using the RANN package. T cell-cancer cell interactions were considered if their centers were between 3 and 25 µm apart, which reduces distant non-interacting cells and artefacts. Then the spot-to-cancer-cell distance was divided by the cell-to-cell distance to calculate the polarization ratio for each interaction pair. Median polarization ratios between conditions and field of views were compared in Graphpad Prism.

Recombinant lentivirus production for CAR T cells

High-titer replication-defective lentivirus was produced and concentrated by ultracentrifugation for primary T cell transduction. Briefly, 24 hours before transfection, HEK-293 cells were seeded at 10×10^6 in 30 mL of medium in a T-150 tissue culture flask. All plasmid DNA was purified using the Endo-free Maxiprep kit (Invitrogen, Life Technologies). HEK-293T cells were transfected with 7 µg pVSV-G (VSV glycoprotein expression plasmid), 18 µg of R874 (Rev and Gag/Pol expression plasmid) and 15 µg of pELNS transgene plasmid, using a mix of Turbofect (Thermo Fisher) and Optimem medium (Invitrogen, Life Technologies, 180 µl of Turbofect for 3 mL of Optimem). The viral supernatant was collected 48 hours after transfection. Viral particles were concentrated by ultracentrifugation for 2 hours at 24,000 x g and resuspended in 400 µl medium, followed by immediate snap freezing on dry ice.

Primary human T cell transduction for CAR T cell generation

Primary human T cells were isolated from the peripheral blood mononuclear cells of healthy donors (HDs; prepared as buffycoats or apheresis filters). All blood samples were collected with informed consent of the healthy donors, and genetically engineered with ethics approval from the Canton of Vaud, Switzerland. PBMC were obtained via Lymphoprep (Axonlab) separation solution, using a standard protocol of centrifugation. CD4 and $CD8^+$ T cells were isolated using a magnetic bead-based negative selection kit following the manufacturer's recommendations (easySEP, Stem Cell technology). Purified CD4 and $CD8^+$ T cells were cultured at a 1:1 ratio and stimulated with anti-CD3

and anti-CD28 Ab coated beads (Invitrogen, Life Technologies) at a ratio of 1:2 T cells to beads. T cells were transduced with lentivirus particles at 18-22 h after activation. Human recombinant IL-2 (h-IL-2; Glaxo) was replenished every other day for a concentration of 50 IU mL^{-1} until 5 days after stimulation (day $^{+}5$). At day $^{+}5$, magnetic beads were removed, and h-IL-7 and h-IL-15 (Miltenyi Biotec) were added to the cultures at 10 ng mL^{-1} replacing h-IL-2. A cell density of 0.5-1 × 10^6 cells mL^{-1} was maintained for expansion. Rested engineered T cells were adjusted for equivalent transgene expression before all functional assays.

Cytotoxicity assay with CAR T cells

Cytotoxicity assays were performed using the IncuCyte Instrument (Essen Bioscience). Briefly, 1.25×10^4 PC3-PIP target cells were seeded in flat bottom 96-well plates (Costar, Vitaris). Four hours later, rested T cells (no cytokine addition for 48 hours) were washed and seeded at 2.5 × 10^4 per well, at a 2:1 effector to target ratio in self-made medium supplemented with 10% dFCS and ±0.6 mM $MgCl_2$. No exogenous cytokines were added during the co-culture period. IncuCyte Caspase-3/7 (Essen Bioscience) was added at a final concentration of 5 µM in a total volume of 200 µl. Internal experimental negative controls were included in all assays, including co-incubation of untransduced (UTD)-T cells and tumor cells in the presence of IncuCyte Caspase-3/7 reagent to monitor spontaneous cell death over time. As a positive control, tumor cells alone were treated with 1% triton solution to evaluate maximal killing in the assay. Images of total green area per well were collected every 2 hours of the co-culture. The total green area per well was obtained by using the same analysis protocol on the IncuCyte ZOOM software provided by Essen Bioscience. Cytotoxicity is reported as total area under the curve of the fluorescence driven by incorporation of cytotoxic green reagent in dead target cells (green area per μm^2). All data were normalized by subtracting the background fluorescence observed at time zero (before any cell killing by CAR T cells) from all further time points.

Cytokine release assay of CAR T cells

Cytokine release assays were performed by co-culture of 5×10^4 T cells with 5×10^4 target cells per well in 96-well round-bottom plates, in duplicate, in a final volume of 200 µl of self-made medium supplemented with 10% dFCS and 0.6 mM $MgCl_2$ or without Mg^{2+} supplementation. After 24 hours, the co-culture supernatants were collected and tested for the presence of IFN-γ by commercial enzyme-linked immunosorbent assay kits according to the manufacturer's protocol (BioLegend).

CAR T cell *in vivo* experiment

Male NSG mice of 10-12 weeks were put on Mg^{2+}-restricted or matching control diet 5 days prior to tumor injection and kept on respective diet throughout the experiment. 5×10^6 PC3-PIP tumor cells were injected subcutaneously. After 5 days, intravenous injection of saline solution or 2×10^6 T cells (UTD or CAR T cells) were adoptively transferred intravenously. Tumor volume was monitored twice

per week. The animals were monitored daily and the tumors were calipered every other day. Tumor volumes were calculated using the formula $V = 1/2(\text{length} \times \text{width}^2)$, where length is the greatest longitudinal diameter and width is the greatest transverse diameter determined via caliper measurement.

Statistical analysis

Statistical significance was tested for using Prism 8.0 (GraphPad Software, USA). P values of less than 0.05 were considered statistically significant.

Supplemental Table 1: crRNA Sequences

Design ID	Species	Position	Strand	Sequence	PAM
Hs.Cas9.ITGAL.1.AA	Human	30475350	-	TGCCCGACTGGCACTGATAG	AGG
Mm.Cas9.ITGAL.1.AB	Mouse	127302137	-	CACATAGTTGATGGCACGAA	AGG

SUPPLEMENTARY MATERIAL

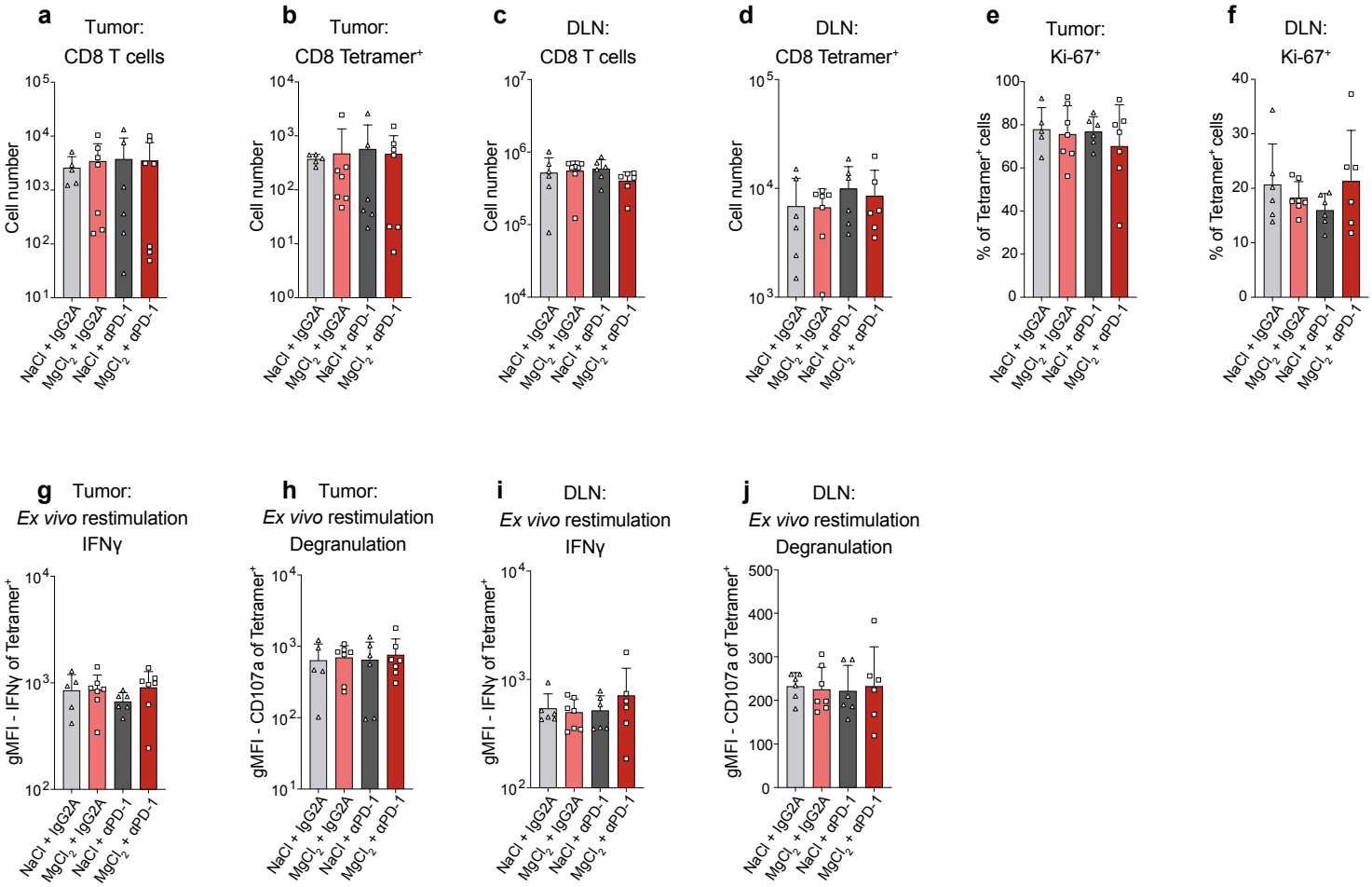
a
Tumor:
CD8 T cells
Cell number
b
Tumor:
CD8 Tetramer+
Cell number
c
DLN:
CD8 T cells
Cell number
d
DLN:
CD8 Tetramer+
Cell number
e
Tumor:
Ki-67+
% of Tetramer+ cells
f
DLN:
Ki-67+
% of Tetramer+ cells
g
Tumor:
Ex vivo restimulation
IFNγ
gMFI - IFNγ of Tetramer+
h
Tumor:
Ex vivo restimulation
Degranulation
gMFI - CD107a of Tetramer+
i
DLN:
Ex vivo restimulation
IFNγ
gMFI - IFNγ of Tetramer+
j
DLN:
Ex vivo restimulation
Degranulation
gMFI - CD107a of Tetramer+
NaCl + IgG2A
MgCl2 + IgG2A
NaCl + αPD-1
MgCl2 + αPD-1

Supplementary Figure 1: Intratumoral magnesium application does not impact $CD8^+$ T cell proliferation *in vivo* and *ex vivo* re-stimulation capacity. (**a**) Cell frequency of tumor-infiltrating (**b**) $CD8^+$ T cells and (**c**) OVA-tetramer specific $CD8^+$ T cells across different treatment groups. Absolute cell numbers of (**c**) $CD8^+$ T cells and (**d**) OVA-tetramer specific $CD8^+$ T cells in tumor-draining lymph node (DLN). Rate of Ki-67 positive, OVA-tetramer specific $CD8^+$ T cells in tumor (**e**) and tumor-draining lymph node (**f**). (**g** – **j**) Flow cytometric analysis of OVA-tetramer specific $CD8^+$ T cells 4 h after *ex vivo* re-stimulation with PMA and ionomycin. Expression levels of IFNγ (**g**) and CD107a (**h**) in tumor-infiltrating antigen-specific $CD8^+$ T cells and expression levels of IFNγ (**i**) and CD107a (**j**) in antigen-specific $CD8^+$ T cells from tumor-draining lymph node.

Each symbol represents an individual mouse, n = 5 – 7 per group. Data is presented as mean $^+$SD. Statistical significance was assessed by one-way ANOVA with Sidak's multiple comparison test. $p < 0.05$, $^{**}p < 0.01$, $^{***}p < 0.001$, $^{****}p < 0.0001$

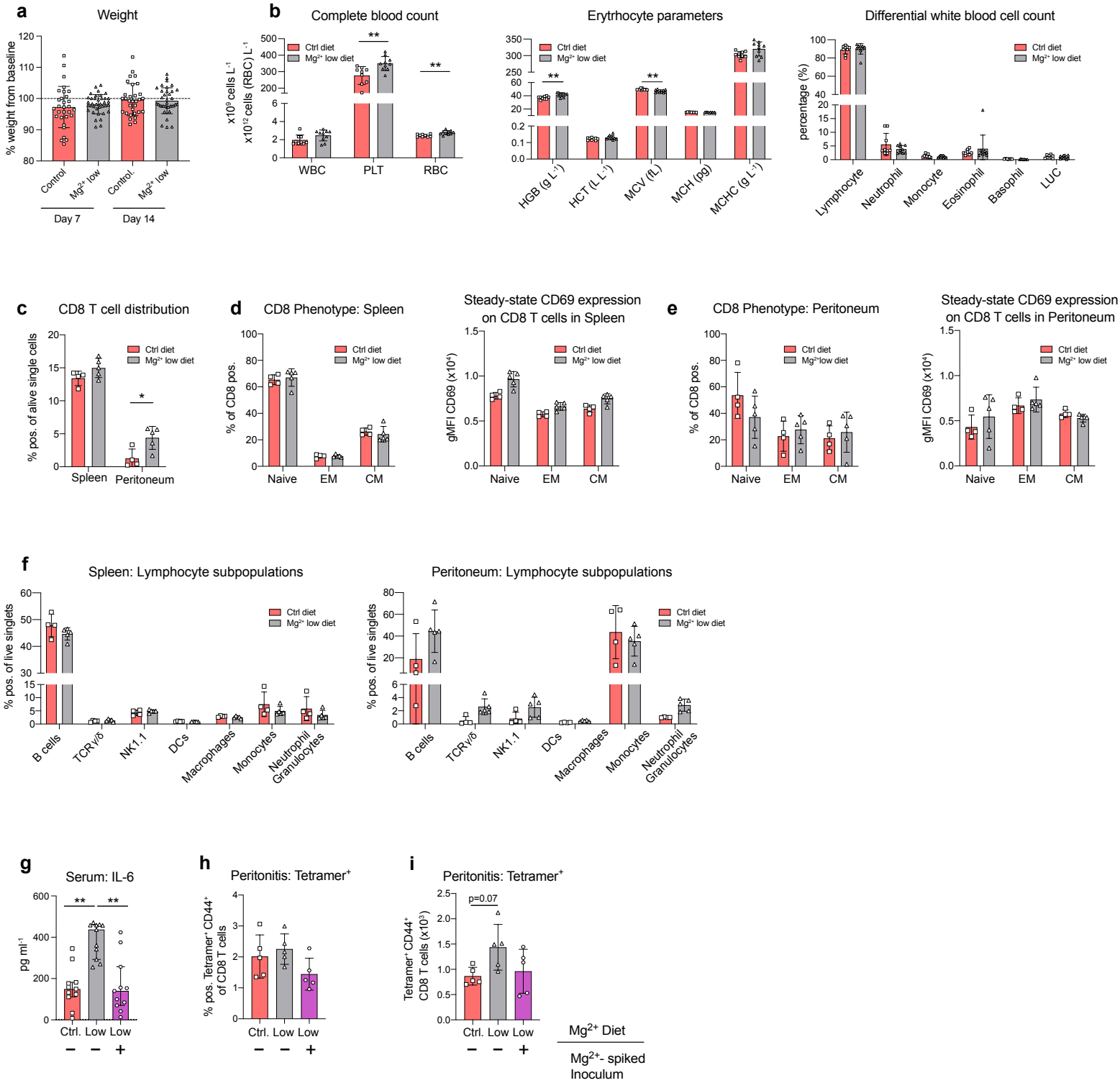
a
Weight
% weight from baseline
Control
Mg2+ low
Control
Mg2+ low
Day 7
Day 14
b
Complete blood count
x10^9 cells L^-1
x10^12 cells (RBC) L^-1
Ctrl diet
Mg2+ low diet
WBC
PLT
RBC
Erytrhocyte parameters
HGB (g L^-1)
HCT (L L^-1)
MCV (fL)
MCH (pg)
MCHC (g L^-1)
Differential white blood cell count
percentage (%)
Lymphocyte
Neutrophil
Monocyte
Eosinophil
Basophil
LUC
c
CD8 T cell distribution
% pos. of alive single cells
Spleen
Peritoneum
d
CD8 Phenotype: Spleen
% of CD8 pos.
Naive
EM
CM
Steady-state CD69 expression on CD8 T cells in Spleen
gMFI CD69 (x10^4)
e
CD8 Phenotype: Peritoneum
Steady-state CD69 expression on CD8 T cells in Peritoneum
f
Spleen: Lymphocyte subpopulations
Peritoneum: Lymphocyte subpopulations
% pos. of live singlets
B cells
TCRγ/δ
NK1.1
DCs
Macrophages
Monocytes
Neutrophil Granulocytes
g
Serum: IL-6
pg ml^-1
Ctrl. Low Low
h
Peritonitis: Tetramer+
% pos. Tetramer+ CD44+ of CD8 T cells
i
Peritonitis: Tetramer+
p=0.07
Tetramer+ CD44+ CD8 T cells (x10^3)
Mg2+ Diet
Mg2+- spiked Inoculum

Supplementary Figure 2: Short-term organismal magnesium depletion via dietary restriction exhibits mild effects on uninfected mice. (**a - k**) Heathy Bl/6 mice were placed on Mg^{2+}-low and matching control diet for 2 weeks without further intervention. (**a**) Dot plot indicating percentage weight change compared to individual baseline value after 7 and 14 days. Pooled data of 4 independent experiments. (**b**) *Left panel*, complete blood count representing absolute numbers of white blood cells (WBC), platelets (PLT) and red blood cells (RBC). *Middle panel*, quantitation of red blood cell parameters: Hemoglobin (HGB), hematocrit (HCT), mean cell volume (MCV), mean cell hemoglobin (MCH), mean cell hemoglobin concentration (MCHC). *Right panel*, different types of white blood cells in peripheral blood are given as percentage distribution. Pooled data of 2 independent experiments. (**c**) Abundance of $CD8^+$ T cells in spleen and peritoneal cavity. (**d** and **e**) Flow cytometric characterization of $CD8^+$ T cell subsets: naïve, effector-memory (EM) and central-memory (CM). Composition of $CD8^+$ T cell subsets in spleen (**d**, *left panel*) and peritoneal cavity (**e**, *left panel*). Quantification of steady-state CD69 expression on $CD8^+$ T cell subsets in spleen (**d**, *right panel*) and peritoneal cavity (**e**, *right panel*). (**f**) Analysis of relative abundance of lymphocyte subpopulations in spleen (*left panel*) and peritoneal cavity (*right panel*). (**g** - **m**) LmOVA infection epxeriments (**g**) Bar graph representing serum IFNγ concentrations among treatment groups. Dashed lines indicate detection limit. Relative abundance (**h**) and absolute cell numbers (**i**) of OVA-tetramer specific memory $CD8^+$ T cells in peritoneal cavity.

Each symbol represents an individual mouse. Data is presented as mean ±SD (**a** – **f**) and (**h** – **i**). Median ±IQR is shown in (**g**). Statistical significance was assessed with unpaired two-tailed Student's t test with Holm-Sidak corrected multiple comparison test (**a** – **f**), Kruskal-Wallis test with Dunn's multiple comparison test (**g**) and one-way ANOVA with Sidak corrected multiple comparison test (**g** – **i**). $p < 0.05$, $**p < 0.01$, $*** p < 0.001$, $**** p < 0.0001$

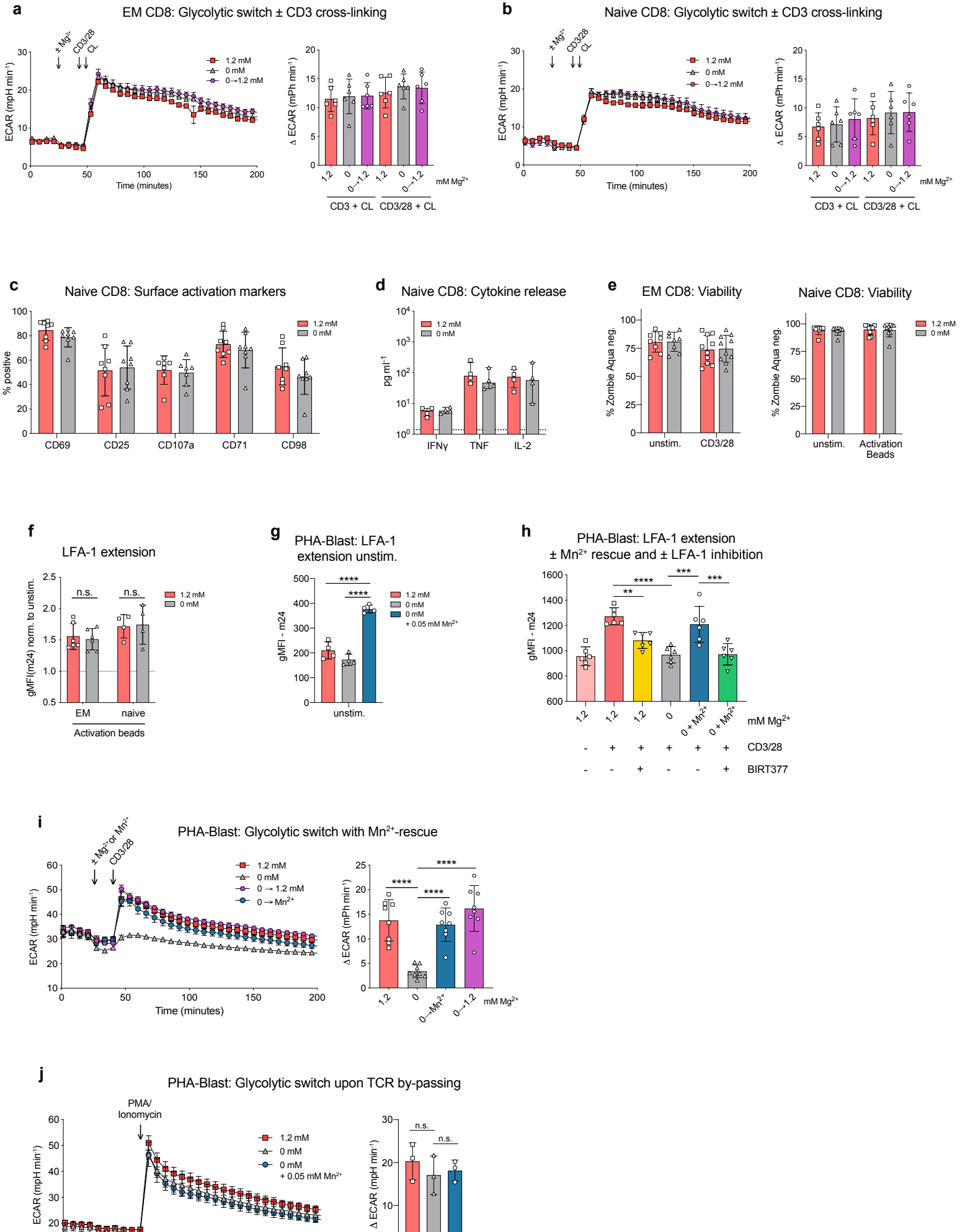
a
EM CD8: Glycolytic switch ± CD3 cross-linking
± Mg2+
CD3/28
CL
1.2 mM
0 mM
0→1.2 mM
ECAR (mpH min-1)
Time (minutes)
Δ ECAR (mPh min-1)
mM Mg2+
CD3 + CL
CD3/28 + CL
b
Naive CD8: Glycolytic switch ± CD3 cross-linking
c
Naive CD8: Surface activation markers
% positive
CD69
CD25
CD107a
CD71
CD98
d
Naive CD8: Cytokine release
pg ml-1
IFNγ
TNF
IL-2
e
EM CD8: Viability
Naive CD8: Viability
% Zombie Aqua neg.
unstim.
CD3/28
Activation Beads
f
LFA-1 extension
gMFI(m24) norm. to unstim.
n.s.
EM
naive
Activation beads
g
PHA-Blast: LFA-1 extension unstim.
gMFI - m24
0 mM + 0.05 mM Mn2+
h
PHA-Blast: LFA-1 extension ± Mn2+ rescue and ± LFA-1 inhibition
0 + Mn2+
CD3/28
BIRT377
i
PHA-Blast: Glycolytic switch with Mn2+-rescue
± Mg2+or Mn2+
0 → Mn2+
0→Mn2+
j
PHA-Blast: Glycolytic switch upon TCR by-passing
PMA/
Ionomycin
+ Mn2+

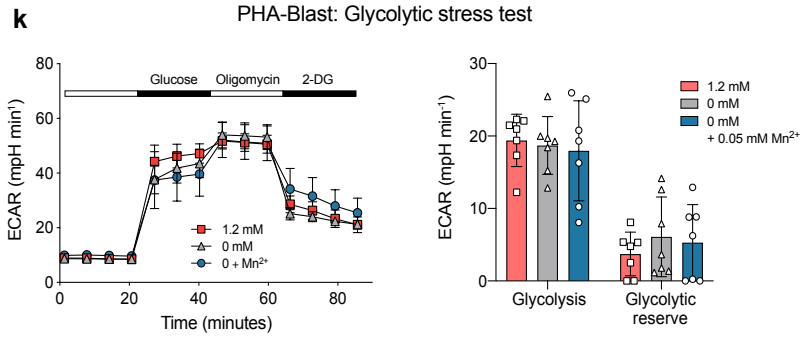
k
PHA-Blast: Glycolytic stress test
Glucose
Oligomycin
2-DG
ECAR (mpH min-1)
Time (minutes)
1.2 mM
0 mM
0 + Mn2+
Glycolysis
Glycolytic reserve
0 mM
+ 0.05 mM Mn2+

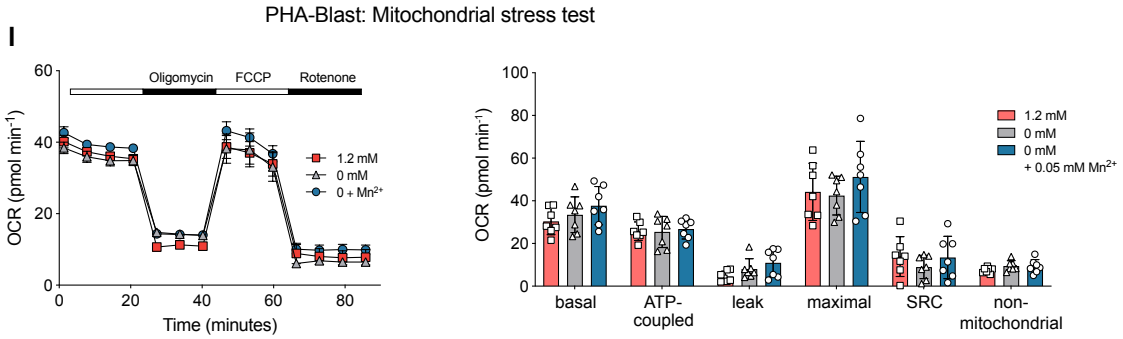
l
PHA-Blast: Mitochondrial stress test
Oligomycin
FCCP
Rotenone
OCR (pmol min-1)
Time (minutes)
basal
ATP-coupled
leak
maximal
SRC
non-mitochondrial

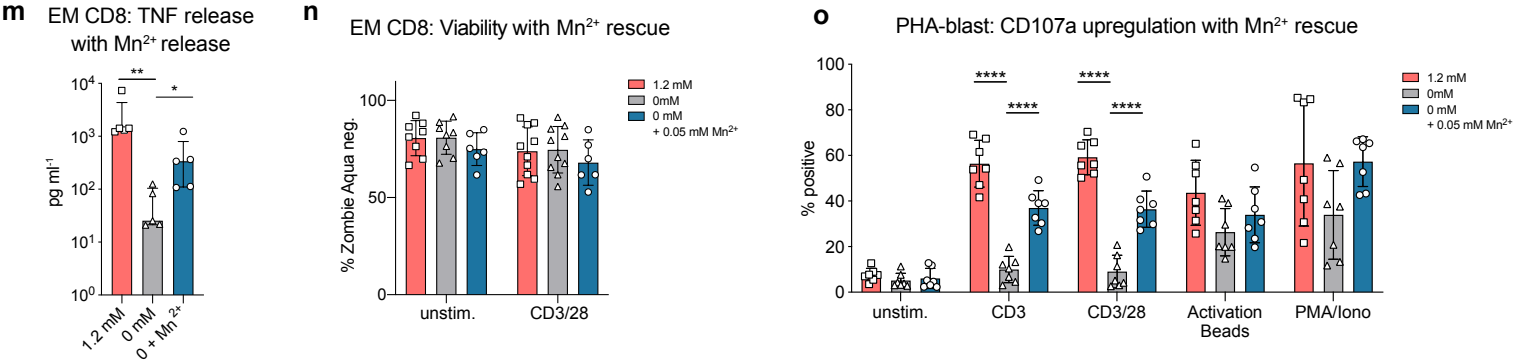
m
EM CD8: TNF release with Mn2+ release
pg ml-1
n
EM CD8: Viability with Mn2+ rescue
% Zombie Aqua neg.
unstim.
CD3/28
o
PHA-blast: CD107a upregulation with Mn2+ rescue
% positive
unstim.
CD3
CD3/28
Activation Beads
PMA/Iono
1.2 mM
0mM
0 mM
+ 0.05 mM Mn2+

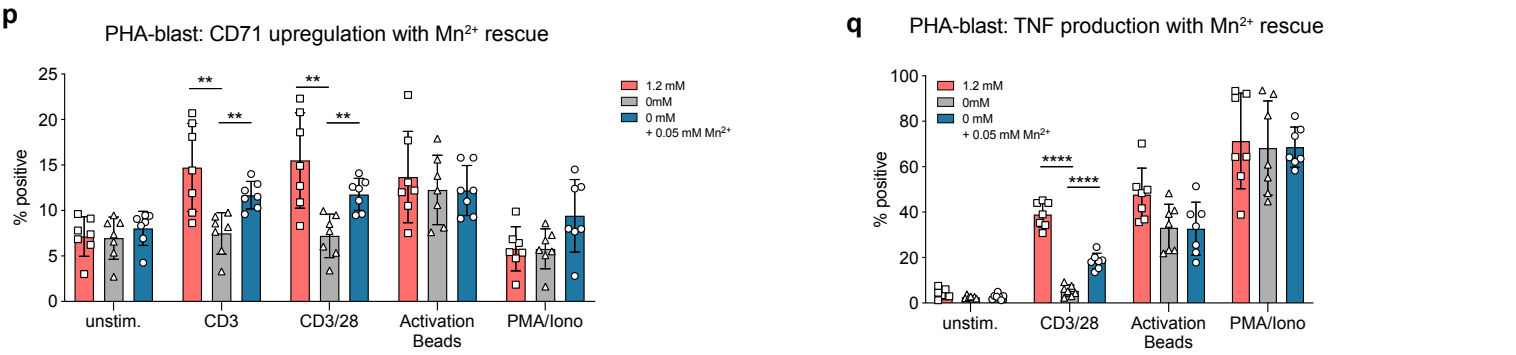
p
PHA-blast: CD71 upregulation with Mn2+ rescue
% positive
unstim.
CD3
CD3/28
Activation Beads
PMA/Iono
q
PHA-blast: TNF production with Mn2+ rescue
1.2 mM
0mM
0 mM
+ 0.05 mM Mn2+

Supplementary Figure 3: Extracellular divalent cations fine-tune T cell activation via LFA-1. (**a**) and (**b**) Activation-induced glycolytic switch of human $CD8^+$ T cell subsets upon additional injection of secondary, cross-linking anti-CD3/28 Ab in medium containing either 1.2 mM Mg^{2+}, 0 mM Mg^{2+}, or medium which was reconstituted from 0 mM to 1.2 mM Mg^{2+} immediately prior to activation (0→1.2 mM Mg^{2+}). (**a**) Results for human effector memory (EM) and (**b**) for human naïve $CD8^+$ T cells. A representative metabolic trace (*left panel*), and pooled data from 3 independent experiments (*right panel*). (**c**) Surface marker expression on activated human naïve $CD8^+$ T cells. Pooled data from 4 independent experiments. (**d**) Abundance of inflammatory cytokines in corresponding cell culture supernatants. Dashed lines indicate detection limit. (**e**) Viability of $CD8^+$ T cell subpopulations after culturing for 24 h. *Left panel* summarizes results from EM $CD8^+$ T cells and *right panel* from naïve $CD8^+$ T cells. Pooled data from > 3 independent experiments. (**f**) TCR activation-induced LFA-1 extension on human EM and naïve $CD8^+$ T cells. Pooled data of 2-3 independent experiments. (**g**) LFA-1 extension on unstimulated human PHA-blasts. (**h**) LFA-1 extension on human PHA T cell blasts. Cells were incubated ± anti-CD3/28 Ab, ± a small-molecule CD11a inhibitor (BIRT377 50 µM). (**i**) Assessment of activation-induced glycolytic switch of human PHA-blasts. Medium in all conditions was initially devoid of Mg^{2+} and, immediately prior to stimulation reconstituted to 1.2 mM Mg^{2+}, 0.05 mM Mn^{2+} – or kept at 0 mM Mg^{2+}, as indicated. One representative experiment (*left panel*) and pooled data from 2 independent experiments (*right panel*) are shown. (**j**) Glycolytic switching of human PHA-blasts upon PMA and ionomycine injection. (**k**) Assessment of glycolysis and glycolytic reserve of human PHA-blasts. One representative experiment (*left panel*) and pooled data from 2 independent experiments (*right panel*) are shown. (**l**) Mitochondrial perturbation assay was with human PHA-blasts. *Left panel* depicting representative experiment and summary bar graph in *right panel* representing calculated basal respiration, ATP-coupled respiration, leak respiration, maximal respiration, and spare respiratory capacity (SRC) as well non-mitochondrial respiration (pooled data from 2 independent experiments). (**m**) Activation-induced TNF release of human EM $CD8^+$ T cells. (**n**) Flow cytometry-based analysis of EM $CD8^+$ T cell viability. Of note, values of 1.2 and 0 mM Mg^{2+} conditions are also depicted in (**e**) since data stems from the same set of experiments. (**o** - **q**) Bar graphs depicting upregulation of degranulation marker CD107a (**p**) and CD71 (**q**) as well TNF production (**q**) in human PHA-blasts upon different activation regimens. Pooled data from 2 independent experiments.

Each symbol represents an individual healthy donor, bars indicate mean ± SD with the exceptions of (**k**) and (**m**) where median ±IQR is shown. In representative metabolic flux analysis symbols indicate mean ±SEM *left panel* of (**a**, **b**, **i**, **j**, **k**, **l**). Statistical significance was assessed with repeated-measures one-way ANOVA with Sidak's multiple comparison test (**a**, **b**), unpaired two-tailed Student's t test with

Holm-Sidak corrected multiple comparison test (**c**, **d**, **e**, **f**, **k**, **l**, **n**, **o**, **p** ,**q**) and one-way ANOVA with Sidak's multiple comparison test (**g**, **h**, **i**, **j**, **m**). *p < 0.05, **p <0.01, *** p < 0.001, **** p < 0.0001

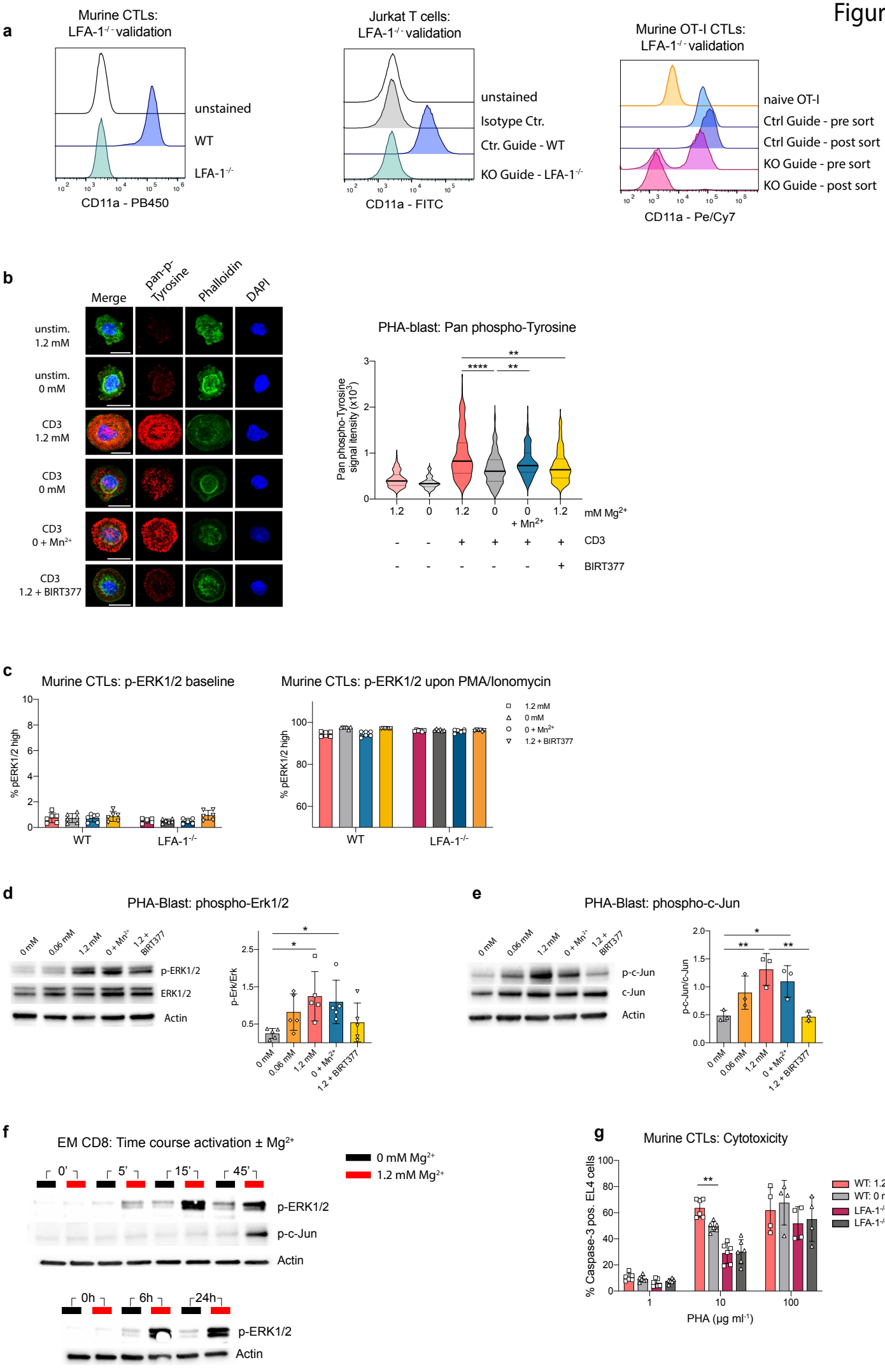
a
Murine CTLs: LFA-1-/- validation
unstained
WT
LFA-1-/-
CD11a - PB450
Jurkat T cells: LFA-1-/- validation
unstained
Isotype Ctr.
Ctr. Guide - WT
KO Guide - LFA-1-/-
CD11a - FITC
Murine OT-I CTLs: LFA-1-/- validation
naive OT-I
Ctrl Guide - pre sort
Ctrl Guide - post sort
KO Guide - pre sort
KO Guide - post sort
CD11a - Pe/Cy7
b
Merge
pan-p-Tyrosine
Phalloidin
DAPI
unstim. 1.2 mM
unstim. 0 mM
CD3 1.2 mM
CD3 0 mM
CD3 0 + Mn2+
CD3 1.2 + BIRT377
PHA-blast: Pan phospho-Tyrosine
Pan phospho-Tyrosine signal itensity (x10^3)
mM Mg2+
+ Mn2+
CD3
BIRT377
c
Murine CTLs: p-ERK1/2 baseline
% pERK1/2 high
WT
LFA-1-/-
Murine CTLs: p-ERK1/2 upon PMA/Ionomycin
1.2 mM
0 mM
0 + Mn2+
1.2 + BIRT377
d
PHA-Blast: phospho-Erk1/2
p-ERK1/2
ERK1/2
Actin
p-Erk/Erk
e
PHA-Blast: phospho-c-Jun
p-c-Jun
c-Jun
Actin
p-c-Jun/c-Jun
f
EM CD8: Time course activation ± Mg2+
0 mM Mg2+
1.2 mM Mg2+
p-ERK1/2
p-c-Jun
Actin
p-ERK1/2
Actin
g
Murine CTLs: Cytotoxicity
% Caspase-3 pos. EL4 cells
PHA (µg ml-1)
WT: 1.2 mM
WT: 0 mM
LFA-1-/-: 1.2 mM
LFA-1-/-: 0 mM

Supplementary Figure 4: Magnesium-LFA-1 axis regulates assembly of proximal TCR signalosome. (**a**) Representative histogram comparing CD11a surface expression on CTLs derived from murine WT and LFA-$1^{-/-}$ CTLs (*left panel*), WT (treated with negative control guide RNA) and LFA-$1^{-/-}$ Jurkat T cells (*middle panel*) as well naïve OT-I cells and CRISPR-Cas9 edited OT-I CTLs before and after purification by cell sorting (*right panel*). (**b**) *Left panel*, representative immunofluorescent images of PHA-blasts stimulated for 2 min on ± anti-CD3-coated coverslip. Cells were stained for pan-tyrosine phosphorylation, actin and nuclei. Images are displayed as confocal projections of 3D stacks. Scale bars indicate 10 µm. *Right panel*, quantitative analysis of fluorescent signal intensity (n = 91 - 146 cells/condition, pooled from 2 - 4 different field of views). (**c**) Flow cytometric analysis of ERK1/2 phosphorylation in murine WT and LFA-$1^{-/-}$ CTLs. *Left panel* showing unstimulated baseline ERK1/2 phosphorylation, *right panel* depicts phosphorylation status upon PMA and ionomycin treatment. Quantified results of n=3 mice in duplicates each. (**d**) and (**e**) Immunoblot analysis of ERK1/2 phosphorylation (**d**) and c-Jun phosphorylation (**e**) in human PHA-blasts. *Left panel* depicting immunoblots being probed for respective phosphorylated and total protein as well actin. *Right panel* illustrating summarized quantitation with 3 – 5 healthy donors. (**f**) Representative immunoblots of primary human EM $CD8^+$ T cells. Immunoblots were probed for phosphorylated ERK1/2 and c-Jun as well actin. (**g**) Caspase-3 activity in EL4 target cells after co-culture with murine WT and LFA-$1^{-/-}$ CTLs at indicated PHA concentrations. Pooled results from 2 independent experiments.

Bars indicate mean ± SD (**c**, **d**, **e**, **g**) and median ±IQR is shown in (**b**). Statistical significance was assessed with Kruskal-Wallis test with Dunn's multiple comparison test (**b**) and one-way ANOVA with Sidak's multiple comparison test (**d**, **e**, **g**). *$p < 0.05$, **$p < 0.01$, *** $p < 0.001$, **** $p < 0.0001$

a

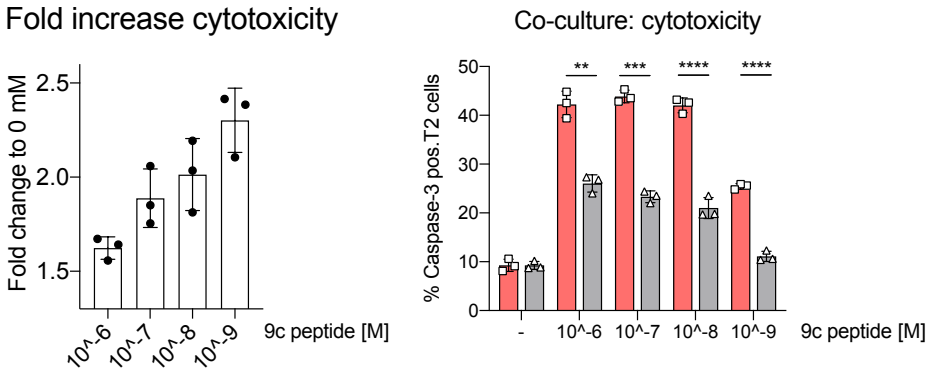
Fold increase cytotoxicity
Fold change to 0 mM
2.5
2.0
1.5
10^-6
10^-7
10^-8
10^-9
9c peptide [M]
Co-culture: cytotoxicity
% Caspase-3 pos.T2 cells
50
40
30
20
10
0
**
***
****
****
-
10^-6
10^-7
10^-8
10^-9
9c peptide [M]

Supplementary Figure 5: Extracellular magnesium augments cytotoxic effector function of REP T cells in low range stimulus. (**a**) Caspase-3 activity in T2 target cells after co-incubation with NY-ESO-1-specific REP T cells. *Left panel* depicts fold increase of caspase-3 positive T2 cells in 1.2 mM Mg^{2+} and *right panel* illustrates corresponding relative

Bars indicate mean ± SD and statistical significance was assessed with unpaired two-tailed Student's t test with Holm-Sidak corrected multiple comparison test (**a** *right panel*). $p < 0.05$, **$p < 0.01$, *** $p < 0.001$, **** $p < 0.0001$

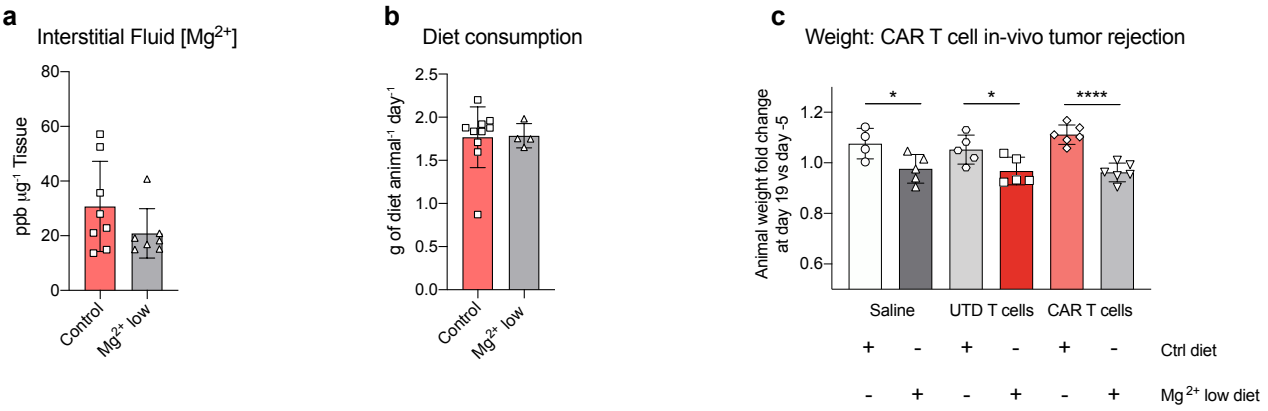

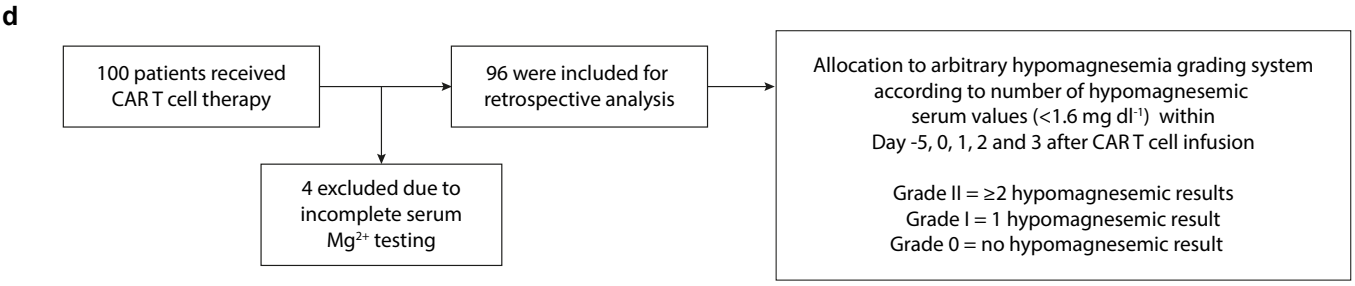

e

Baseline Characterstics

	Overall (N=96)	Grade 0 (N=80)	Grade I (N=11)	Grade II (N=5)
Male sex - no. (%)	70 (72.9)	57 (71.3)	9 (81.8)	4 (80.0)
Age - years				
Mean ±SD	57.1±14.8	57.8±15.2	50.9±14.2	58.0±3.3
Median (IQR)	60 (50.5-67)	60.5 (51.3-67.8)	53 (47.0-64.0)	57 (55.5-61.0)
Disease Type - no. (%)				
DLBCL	73 (76.0)	60 (75.0)	9 (81.8)	4 (80.0)
PMBCL	6 (6.3)	6 (7.5)	0 (0.0)	0 (0.0)
TFL	17 (17.7)	14 (17.5)	2 (18.2)	1 (20.0)
ECOG performance-status of 0 or 1				
- no. (%)	87 (90.6)	73 (91.3)	10 (90.9)	4 (80.0)
Disease Stage - no. (%)				
I or II	15 (18.5)	13 (16.3)	1 (9.1)	1 (20.0)
III or IV	81 (84.4)	67 (83.8)	10 (90.9)	4 (80.0)

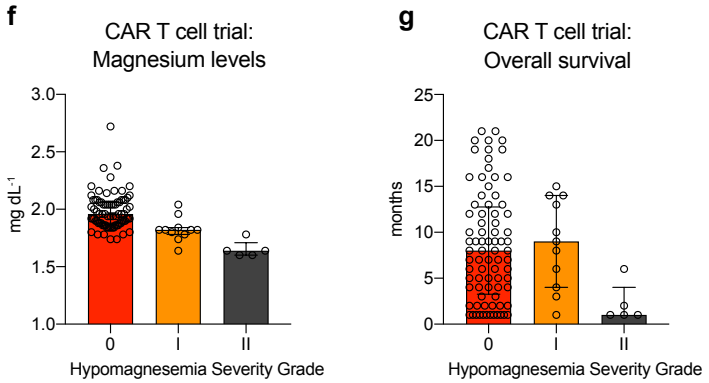

Supplementary Figure 6: Extracellular magnesium shapes CAR T cell functionality *in vitro* and *in vivo.* (**a**) Magnesium levels determined by ICP-MS in interstitial fluid of tumors from UTD and saline control mice reaching ethically acceptable end point. (**b**) Diet consumption of mice in CAR T cell tumor rejection experiment. (**c**) Dot plot indicating fold change in body weight after 19 days of respective diet normalized to individual starting value. (**a** – **c**) Each symbol represents one mouse. (**d**) Study work flow and patient exclusion criteria. (**e**) Table with baseline characteristics. Abbreviations: Diffuse large B-cell lymphoma (DLBCL), Primary mediastinal large B-cell lymphoma (PMCL) and Transformed Follicular Lymphoma (TFL). (**f**) Comparison of mean serum magnesium levels among three grades of hypomagnesemia severity score over 5 initial measurements. (**g**) Overall survival of patients allocated to different hypomagnesemia severity grading. (**f** – **g**) Each symbol represents individual patient.

Bars indicate mean ±SD (**a**, **b**, **c**) and median ±IQR (**f**, **g**). Statistical significance was determined with unpaired two-tailed Student's t test (**a**, **b**) and one-way ANOVA with Sidak's multiple comparison test (**c**). $p < 0.05$, $^{**}p < 0.01$, $^{***}p < 0.001$, $^{****}p < 0.0001$.

REFERENCES

1 Elin, R. J. Magnesium: the fifth but forgotten electrolyte. *Am J Clin Pathol* **102**, 616-622, doi:10.1093/ajcp/102.5.616 (1994).

2 Jahnen-Dechent, W. & Ketteler, M. Magnesium basics. *Clinical Kidney Journal* **5**, i3-i14, doi:10.1093/ndtplus/sfr163 (2012).

3 de Baaij, J. H., Hoenderop, J. G. & Bindels, R. J. Magnesium in man: implications for health and disease. *Physiol Rev* **95**, 1-46, doi:10.1152/physrev.00012.2014 (2015).

4 Romani, A. M. P. in *Interrelations between Essential Metal Ions and Human Diseases* (eds Astrid Sigel, Helmut Sigel, & Roland K. O. Sigel) 49-79 (Springer Netherlands, 2013).

5 Kanellopoulou, C. *et al.* Mg(2+) regulation of kinase signaling and immune function. *J Exp Med* **216**, 1828-1842, doi:10.1084/jem.20181970 (2019).

6 Saris, N.-E. L., Mervaala, E., Karppanen, H., Khawaja, J. A. & Lewenstam, A. Magnesium: An update on physiological, clinical and analytical aspects. *Clinica Chimica Acta* **294**, 1-26, doi:https://doi.org/10.1016/S0009-8981(99)00258-2 (2000).

7 Costello, R. B. & Nielsen, F. Interpreting magnesium status to enhance clinical care: key indicators. *Curr Opin Clin Nutr Metab Care* **20**, 504-511, doi:10.1097/MCO.0000000000000410 (2017).

8 Schulze, M. B. *et al.* Fiber and magnesium intake and incidence of type 2 diabetes: a prospective study and meta-analysis. *Arch Intern Med* **167**, 956-965, doi:10.1001/archinte.167.9.956 (2007).

9 Qu, X. *et al.* Magnesium and the risk of cardiovascular events: a meta-analysis of prospective cohort studies. *PLoS One* **8**, e57720, doi:10.1371/journal.pone.0057720 (2013).

10 Larsson, S. C., Orsini, N. & Wolk, A. Dietary magnesium intake and risk of stroke: a meta-analysis of prospective studies. *Am J Clin Nutr* **95**, 362-366, doi:10.3945/ajcn.111.022376 (2012).

11 Sojka, J. Magnesium supplementation and osteoporosis. *Nutrition reviews* **53**, 71-74 (1995).

12 Ravell, J. *et al.* Plasma magnesium is inversely associated with Epstein-Barr virus load in peripheral blood and Burkitt lymphoma in Uganda. *Cancer Epidemiol* **52**, 70-74, doi:10.1016/j.canep.2017.12.004 (2018).

13 Sakaguchi, Y. *et al.* Hypomagnesemia is a significant predictor of cardiovascular and non-cardiovascular mortality in patients undergoing hemodialysis. *Kidney Int* **85**, 174-181, doi:10.1038/ki.2013.327 (2014).

14 Kieboom, B. C. *et al.* Proton pump inhibitors and hypomagnesemia in the general population: a population-based cohort study. *Am J Kidney Dis* **66**, 775-782, doi:10.1053/j.ajkd.2015.05.012 (2015).

15 Martin, B. J., Black, J. & McLelland, A. S. Hypomagnesaemia in elderly hospital admissions: a study of clinical significance. *Q J Med* **78**, 177-184 (1991).

16 Wong, E. T., Rude, R. K., Singer, F. R. & Shaw, S. T., Jr. A high prevalence of hypomagnesemia and hypermagnesemia in hospitalized patients. *Am J Clin Pathol* **79**, 348-352, doi:10.1093/ajcp/79.3.348 (1983).

17 Cheungpasitporn, W., Thongprayoon, C. & Qian, Q. Dysmagnesemia in Hospitalized Patients: Prevalence and Prognostic Importance. *Mayo Clin Proc* **90**, 1001-1010, doi:10.1016/j.mayocp.2015.04.023 (2015).

18 Ryzen, E., Wagers, P. W., Singer, F. R. & Rude, R. K. Magnesium deficiency in a medical ICU population. *Critical Care Medicine* **13**, 19-21, doi:10.1097/00003246-198501000-00006 (1985).

19 Chernow, B. *et al.* Hypomagnesemia in Patients in Postoperative Intensive Care. *Chest* **95**, 391-397, doi:https://doi.org/10.1378/chest.95.2.391 (1989).

20 Velissaris, D., Karamouzos, V., Pierrakos, C., Aretha, D. & Karanikolas, M. Hypomagnesemia in Critically Ill Sepsis Patients. *J Clin Med Res* **7**, 911-918, doi:10.14740/jocmr2351w (2015).

21 Nasulewicz, A. *et al.* Magnesium deficiency inhibits primary tumor growth but favors metastasis in mice. *Biochim Biophys Acta* **1739**, 26-32, doi:10.1016/j.bbadis.2004.08.003 (2004).

22 Brenner, M., Laragione, T. & Gulko, P. S. Short-term low-magnesium diet reduces autoimmune arthritis severity and synovial tissue gene expression. *Physiol Genomics* **49**, 238-242, doi:10.1152/physiolgenomics.00003.2017 (2017).

23 Martin, M. D. & Badovinac, V. P. Defining Memory CD8 T Cell. *Front Immunol* **9**, 2692, doi:10.3389/fimmu.2018.02692 (2018).

24 Martín-Cófreces, N. B., Baixauli, F. & Sánchez-Madrid, F. Immune synapse: conductor of orchestrated organelle movement. *Trends Cell Biol* **24**, 61-72, doi:10.1016/j.tcb.2013.09.005 (2014).

25 Dustin, M. L. & Long, E. O. Cytotoxic immunological synapses. *Immunol Rev* **235**, 24-34, doi:10.1111/j.0105-2896.2010.00904.x (2010).

26 Dieckmann, N. M., Frazer, G. L., Asano, Y., Stinchcombe, J. C. & Griffiths, G. M. The cytotoxic T lymphocyte immune synapse at a glance. *J Cell Sci* **129**, 2881-2886, doi:10.1242/jcs.186205 (2016).

27 Lötscher, J. & Balmer, M. L. Sensing between reactions - how the metabolic microenvironment shapes immunity. *Clin Exp Immunol* **197**, 161-169, doi:10.1111/cei.13291 (2019).

28 Bantug, G. R., Galluzzi, L., Kroemer, G. & Hess, C. The spectrum of T cell metabolism in health and disease. *Nat Rev Immunol* **18**, 19-34, doi:10.1038/nri.2017.99 (2018).

29 Chapman, N. M., Boothby, M. R. & Chi, H. Metabolic coordination of T cell quiescence and activation. *Nature Reviews Immunology* **20**, 55-70, doi:10.1038/s41577-019-0203-y (2020).

30 Kedia-Mehta, N. & Finlay, D. K. Competition for nutrients and its role in controlling immune responses. *Nature Communications* **10**, 2123, doi:10.1038/s41467-019-10015-4 (2019).

31 Vorup-Jensen, T., Waldron, T. T., Astrof, N., Shimaoka, M. & Springer, T. A. The connection between metal ion affinity and ligand affinity in integrin I domains. *Biochim Biophys Acta* **1774**, 1148-1155, doi:10.1016/j.bbapap.2007.06.014 (2007).

32 van Aalderen, M. C. *et al.* Label-free Analysis of CD8(+) T Cell Subset Proteomes Supports a Progressive Differentiation Model of Human-Virus-Specific T Cells. *Cell Rep* **19**, 1068-1079, doi:10.1016/j.celrep.2017.04.014 (2017).

33 Hogg, N., Patzak, I. & Willenbrock, F. The insider's guide to leukocyte integrin signalling and function. *Nature Reviews Immunology* **11**, 416-426, doi:10.1038/nri2986 (2011).

34 Zhang, K. & Chen, J. The regulation of integrin function by divalent cations. *Cell Adhesion & Migration* **6**, 20-29, doi:10.4161/cam.18702 (2012).

35 Schürpf, T. & Springer, T. A. Regulation of integrin affinity on cell surfaces. *The EMBO Journal* **30**, 4712-4727, doi:10.1038/emboj.2011.333 (2011).

36 Semmrich, M. *et al.* Importance of integrin LFA-1 deactivation for the generation of immune responses. *J Exp Med* **201**, 1987-1998, doi:10.1084/jem.20041850 (2005).

37 Trebak, M. & Kinet, J.-P. Calcium signalling in T cells. *Nature Reviews Immunology* **19**, 154-169, doi:10.1038/s41577-018-0110-7 (2019).

38 Hoth, M., Button, D. C. & Lewis, R. S. Mitochondrial control of calcium-channel gating: A mechanism for sustained signaling and transcriptional activation in T lymphocytes. *Proceedings of the National Academy of Sciences* **97**, 10607-10612, doi:10.1073/pnas.180143997 (2000).

39 Quintana, A. *et al.* T cell activation requires mitochondrial translocation to the immunological synapse. **104**, 14418-14423, doi:10.1073/pnas.0703126104 (2007).

40 Contento, R. L. *et al.* Adhesion shapes T cells for prompt and sustained T-cell receptor signalling. *The EMBO Journal* **29**, 4035-4047, doi:10.1038/emboj.2010.258 (2010).

41 Li, D., Molldrem, J. J. & Ma, Q. LFA-1 Regulates CD8+T Cell Activation via T Cell Receptor-mediated and LFA-1-mediated Erk1/2 Signal Pathways. *Journal of Biological Chemistry* **284**, 21001-21010, doi:10.1074/jbc.m109.002865 (2009).

42 Dudley, M. E. *et al.* Cancer Regression and Autoimmunity in Patients After Clonal Repopulation with Antitumor Lymphocytes. *Science* **298**, 850-854, doi:10.1126/science.1076514 (2002).

43 Thomas, R. *et al.* NY-ESO-1 Based Immunotherapy of Cancer: Current Perspectives. *Front Immunol* **9**, 947-947, doi:10.3389/fimmu.2018.00947 (2018).

44 Santoro, S. P. *et al.* T cells bearing a chimeric antigen receptor against prostate-specific membrane antigen mediate vascular disruption and result in tumor regression. *Cancer Immunol Res* **3**, 68-84, doi:10.1158/2326-6066.Cir-14-0192 (2015).

45 Eil, R. *et al.* Ionic immune suppression within the tumour microenvironment limits T cell effector function. *Nature* **537**, 539-543, doi:10.1038/nature19364 (2016).

46 Kleinewietfeld, M. *et al.* Sodium chloride drives autoimmune disease by the induction of pathogenic TH17 cells. *Nature* **496**, 518-522, doi:10.1038/nature11868 (2013).

47 Kanarek, N., Petrova, B. & Sabatini, D. M. Dietary modifications for enhanced cancer therapy. *Nature* **579**, 507-517, doi:10.1038/s41586-020-2124-0 (2020).

48 Lee, C. *et al.* Fasting cycles retard growth of tumors and sensitize a range of cancer cell types to chemotherapy. *Sci Transl Med* **4**, 124ra127, doi:10.1126/scitranslmed.3003293 (2012).

49 Kanarek, N. *et al.* Histidine catabolism is a major determinant of methotrexate sensitivity. *Nature* **559**, 632-636, doi:10.1038/s41586-018-0316-7 (2018).

50 Di Biase, S. *et al.* Creatine uptake regulates CD8 T cell antitumor immunity. *J Exp Med* **216**, 2869-2882, doi:10.1084/jem.20182044 (2019).

51 Whang, R. Magnesium deficiency: pathogenesis, prevalence, and clinical implications. *Am J Med* **82**, 24-29, doi:10.1016/0002-9343(87)90129-x (1987).

52 Liu, W. *et al.* Hypomagnesemia and Survival in Patients with Ovarian Cancer Who Received Chemotherapy with Carboplatin. *Oncologist* **24**, e312-e317, doi:10.1634/theoncologist.2018-0465 (2019).

53 Oronsky, B. *et al.* Electrolyte disorders with platinum-based chemotherapy: mechanisms, manifestations and management. *Cancer Chemother Pharmacol* **80**, 895-907, doi:10.1007/s00280-017-3392-8 (2017).

54 Goodman, S. L. & Picard, M. Integrins as therapeutic targets. *Trends Pharmacol Sci* **33**, 405-412, doi:10.1016/j.tips.2012.04.002 (2012).

55 Semmrich, M. *et al.* Importance of integrin LFA-1 deactivation for the generation of immune responses. *The Journal of experimental medicine* **201**, 1987-1998, doi:10.1084/jem.20041850 (2005).

56 Dransfield, I., Cabanas, C., Barrett, J. & Hogg, N. Interaction of leukocyte integrins with ligand is necessary but not sufficient for function. *The Journal of cell biology* **116**, 1527-1535 (1992).

57 Stephan, M. T., Stephan, S. B., Bak, P., Chen, J. & Irvine, D. J. Synapse-directed delivery of immunomodulators using T-cell-conjugated nanoparticles. *Biomaterials* **33**, 5776-5787 (2012).

58 Zhang, Y. *et al.* Deep single-cell RNA sequencing data of individual T cells from treatment-naïve colorectal cancer patients. *Sci Data* **6**, 131, doi:10.1038/s41597-019-0131-5 (2019).

59 Krutzik, P. O. & Nolan, G. P. Intracellular phospho-protein staining techniques for flow cytometry: monitoring single cell signaling events. *Cytometry A* **55**, 61-70, doi:10.1002/cyto.a.10072 (2003).

60 Heberle, H., Meirelles, G. V., da Silva, F. R., Telles, G. P. & Minghim, R. InteractiVenn: a web-based tool for the analysis of sets through Venn diagrams. *BMC Bioinformatics* **16**, 169, doi:10.1186/s12859-015-0611-3 (2015).

61 Schmid, D. A. *et al.* Evidence for a TCR affinity threshold delimiting maximal CD8 T cell function. *J Immunol* **184**, 4936-4946, doi:10.4049/jimmunol.1000173 (2010).

62 Hebeisen, M. *et al.* Molecular insights for optimizing T cell receptor specificity against cancer. *Front Immunol* **4**, 154, doi:10.3389/fimmu.2013.00154 (2013).